Zeolitic Imidazolate Framework-8 derived ZnO with Polymeric Carbon Nitride for Photocatalytic degradation of Rhodamine B

A project report

Submitted in partial fulfillment of the requirement for the degree of

Master of Science in Chemistry (Inorganic)

BY

VAISHAK T B (011808)

SCHOOL OF CHEMICAL SCIENCES,
MAHATMA GANDHI UNIVERSITY,
KOTTAYAM,
KERALA -686560

Under the guidance of

Prof. (Dr.) SURESH MATHEW

School of Chemical Sciences

Mahatma Gandhi University

Kottayam, Kerala

August 2020

DECLARATION

I**, VAISHAK T B (011808)**, hereby declare that the project report entitled "**Zeolitic Imidazolate Framework-8 derived ZnO with Polymeric Carbon Nitride for Photocatalytic degradation of Rhodamine B"** is a record of original research work carried out by me towards the award of the degree of Master of Science in Inorganic Chemistry. I have completed this study under the supervision of **Prof. (Dr.) Suresh Mathew, School of Chemical Sciences, Mahatma Gandhi University, Kottayam, Kerala.** I, also declare that this report has not been submitted for the award of any degree, diploma, associate ship, fellowship or another title. In accordance with the practice of reporting scientific observations, due acknowledgement has been made whenever the work described is based on the findings of other investigations. Any omission, which might have occurred by oversight or error in judgement, is deeply regretted.

Kottayam
August, 2020

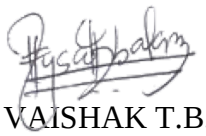

VAISHAK T.B.

School of Chemical Sciences
Mahatma Gandhi University
Priyadarsini Hills P.O - 686 560
Kottayam, Kerala, INDIA
E-mail: *sureshmathewmgu@gmail.com*

CERTIFICATE

This is to certify that the project report entitled "**Zeolitic Imidazolate Framework-8 derived ZnO with Polymeric Carbon Nitride for Photocatalytic degradation of Rhodamine B**" has been carried out by **Mr. VAISHAK T B**, student of Master of Science in Chemistry (Inorganic) from School of Chemical Sciences, Mahatma Gandhi University, Kottayam, Kerala in my research group and under my guidance at School of Chemical Sciences, Mahatma Gandhi University, Kottayam, Kerala starting from June 2020 to August 2020. The research work in the thesis is original research carried out in my lab and same has not been submitted elsewhere.

Prof. (Dr.) Suresh Mathew
School of Chemical Sciences
MG University, Kottayam

SCHOOL OF CHEMICAL SCIENCES
Mahatma Gandhi University
Priyadarsini Hills P. O., Kottayam-686 560
Kerala, India

CERTIFICATE

This is to certify that the work incorporated in this project entitled "**Zeolitic Imidazolate Framework-8 derived ZnO with Polymeric Carbon Nitride for Photocatalytic degradation of Rhodamine B"** submitted by **Mr. VAISHAK T B** for the partial fulfillment of the requirement for the degree of Master of Science in Chemistry (Inorganic Chemistry), to the Director, School of Chemical Sciences, Mahatma Gandhi University, Kottayam, was carried out under the supervision of **Prof. (Dr.) SURESH MATHEW, School Of Chemical Sciences, Mahatma Gandhi University, Kottayam, Kerala, 686560, in** the year 2020.

Dr. K. S. Devaky
The Director
School of Chemical Sciences
MG University, Kottayam

Kottayam
August, 2020

ACKNOWLEDGEMENT

I express my sincere and deep sense of gratitude to my guide **Prof. (Dr.) Suresh Mathew** for providing me with an opportunity to join his team as a project intern at School of chemical sciences, Mahatma Gandhi university. Without his precious support, it would not have been possible to conduct this research. Each meeting with him added invaluable aspects to the implementation and broadened my perspective.

I am extremely thankful to **Dr. K. S. Devaky**, The Director, School of Chemical Sciences, Mahatma Gandhi University, Kottayam, and Kerala for giving me an opportunity to work on this project and providing necessary help at every stage of the project.

I owe my deep sense of gratitude towards **Mrs. Vandana P. V.**, Ph.D. Scholar, for patiently guiding me throughout my work and suggesting me new ideas in the current project. Without her continued interest, immense help and stimulating suggestions, my endeavour to have a successful project would not be fruitful. I am extending my deepest thanks to **Soumya Krishna P, Arsha N Shaji, Nathaniel C Roy, Ananthu Sudheesh, Samjeev P. S. and Monisha R.** for their valuable help and support. I also thank all my other lab mates for their kind cooperation and help.

I would like to thank all my friends for their precious care and support. I also extend my heartfelt thanks to my parents and well-wishers for their love and encouragement.

Finally thanking God almighty for showering his blessings for the successful completion of this project.

VAISHAK T. B.

Contents

1. INTRODUCTION

Nature is a life-sustaining network, in which various living beings exist in harmony. But the human quest for knowledge and development has resulted in the rapid growth of modern technologies, leaving the environment with some serious mark-over. Pollutants are the after-effect of this pacing development which damages stability of ecosystem. So we are now redirecting in a path for nature sustainability.

The uncontrollable increase in waste materials creates considerable damage to the ecosystem. The nature is getting more exposed to harmful threats. And different researches are carrying out for effective measures to remove or reduce nature burden. Heterogeneous photo catalysis using semiconductor, as green technology is generally considered as an effective pathway for the reduction of global environmental pollutants through photocatalytic reaction has received considerable and persistent attention over the last few decades [1]. Hence efficient catalysts are developing for the purpose.

In different industrial processes, organic and inorganic compounds are lost to the waste water and eventually into fresh water, which can then exert devastating effects on the ecosystem due to its stability, toxicity, and non-biodegradability [1,2]. There are different point and non-point sources. Among them industrial effluences, pesticides, dyes, etc. remain as major persistent water pollutants. Photocatalytic reactions use the energy required to convert light energy into a chemical reaction to produce a catalytic effect. Its most representative example in nature is the photosynthesis of plants. Photocatalytic technology can convert organic pollutants into inorganic small molecules such as CO_2 and H_2O: in wastewater treatment, it is considered to be a promising green technology for treating pollutants containing organic, inorganic, and microbial pollutants [3,4]. Semiconductor photocatalytic technology has many advantages over other water treatment technologies, including the variety of contaminants (organic, inorganic, and microbial) that it can remove, as well as the media (liquid and aqueous media) involved in the process [5–7]. To date, the photocatalytic performance of photocatalysts has become a key issue limiting the development of photocatalytic technologies, which are adopted to treat various types of contaminants. Therefore, semiconductor photocatalysts with excellent performance have become a focus of current research. Semiconductor photocatalysts offer the advantages of high efficiency, low energy consumption, and mild reaction conditions [8,9]. In addition, semiconductor photocatalysts can also be used in a variety of applications such as sensors [10], solar cells [11], contaminant adsorption [4], organic synthesis catalysts, and water cracking [12,13]. Among the many semiconductor catalysts, the

wide-band gap semiconductor ZnO with direct band gap exhibits significant photocatalytic activity in various dye solutions [14,15]

1.1. Photocatalysis

Photocatalysis is a type of catalysis that leads to a change in the rate of a photoreaction, a chemical reaction involving the absorption of light by one or more reacting species by adding substances (catalysts) that participate in a chemical reaction without consumption. Photocatalysis, while varying in details in terms of reactions and mechanisms, may be described by four important steps (Fig. 1.1.): (I) light absorption to generate electron-hole pairs; (II) separation of excited charges; (III) transfer of electrons and holes to the surface of photocatalysts; and (IV) utilization of charges on the surface for redox reactions. For the third step, a large portion of electron-hole pairs recombine, either en route to the surface or on the surface sites [16,17,18]. The recombination dissipates the harvested energy in the form of heat (nonradiative recombination) or light emission (radiative recombination) [19]. The long-lived photogenerated charges on the surface have the potential to promote different redox reactions, the details of which depend on the donor or acceptor properties of the surface absorbed species.

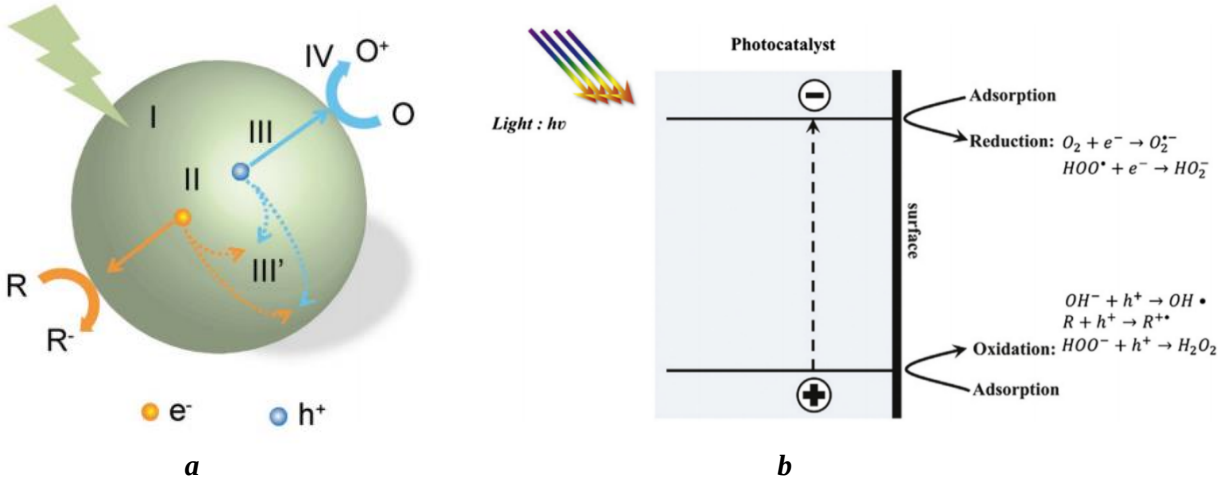

a ***b***

Fig. 1.1.a) *Steps in photocatalytic reaction process. R: chemicals in reductive reactions, O: chemicals in oxidative reactions. (I) light absorption to generate electron-hole pairs; (II) separation of excited charges; (III) transfer of electrons and holes to the surface of photocatalysts; (III) recombination of electrons and holes; (IV) utilization of charges on the surface for redox reactions.* ***b)*** *Schematic representation of mechanism of photocatalysis*

The photocatalyst first absorbs lights with photon energy equal to or higher than its bandgaps, the lone electrons will be excited from valence band (VB) to conduction band (CB). As a result, a photon excited electron-hole pair is formed. After the electron-hole pairs have been formed under light illumination, the charge carriers start to diffuse from inside to the surface of photocatalyst particles. The VB holes and CB electron diffused to the surface of photocatalyst particles are so-called surface-trapped electron and holes, in which they can be exploited for various redox processes. In the presence of oxygen, the photoexcited negative electrons react with the oxygen, as electron acceptor to form superoxides radical $O_2^{-\cdot}$, which could be further protonated to form hydroperoxyl radical ($HO_2^{\cdot}$) and subsequently becoming H_2O_2. The positive holes react with water, an electron donor, to form oxidizing free radicals, · OH. The generated active radicals can then degrade the organic pollutants into final products of CO_2 and H_2O.

Among various renewable energy sources, solar energy is a kind of abundant and clean choice. Thus, solar light-driven technologies for environmental remediation have attracted great attention. The solar energy spectrum is constituted by ∼5% UV light, 42− 45% visible light, and ∼50% near-infrared (NIR) light. It is highly desired to extend the light absorption of photocatalysts from the UV to visible and even the NIR region to achieve improved solar energy utilization. Since, UV light accounts for less than 5% of incident solar light, so the utilization of visible light (nearly 45%) is more promising for better utilization of solar energy and future large-scale practical applications.

There are several type of photocatalytic reactions like photosynthesis, homogeneous photocatalysis, heterogeneous photocatalysis, photoelectroreaction etc. There are many catalysts reported in literatures for this exciting process. Among the metal oxides TiO_2, ZnO, CeO_2 and SnO_2, which are abundant in nature, have also been commonly used as photocatalysts, especially as heterogeneous photocatalysts for several decades. It is attributed to their biocompatibility, excellent durability under a number of conditions and capacity to produce charge carriers when stimulated by the necessary amount of light energy. The desirable combination of electronic composition, light absorption properties, load transport characteristics and energized lifetimes of metal oxides has made it possible for them to be used as photocatalysts. One of the least complicated applications of photocatalysis is to simply suspend photocatalysts in a solution and shine light on it. Often, nanoscale photocatalysts are used. In such a system, each photocatalyst nanoparticle may be regarded as an integrated system consisting of short-circuited photoanode and photocathode. Naturally, the ease of implementation offers the benefit of low cost. The simplicity, nevertheless, also introduces significant challenges, the most critical of which is

the low efficiency [20]. Reasons for the low efficiency include severe recombination [21]. Because the reduction and oxidation sites at the nanoscale in such an integrated system are often not well defined, the charge separation mechanisms are consequently not optimized, thereby resulting in charge recombination within an individual photocatalyst or on the surface or both. The close proximity of the reduction and oxidation sites provides ample opportunities for the reduction intermediates and/or products to be oxidized, and vice versa. Additionally, having a mixture of oxidizing and reducing products (e.g. O_2 and H_2) raises concerns over safety [22]. The separation of the mixture later incurs additional cost.

Heterogeneous photocatalysis is a discipline which includes a large variety of reactions: mild or total oxidations, dehydrogenation, hydrogen transfer, $O_2^{18} – O_2^{16}$ and deuterium-alkane isotopic exchange, metal deposition, water detoxification, gaseous pollutant removal, etc. In line with the two latter points, it can be considered as one of the new 'Advanced Oxidation Technologies' (AOT) for air and water purification treatment [23-28]. Heterogeneous photocatalysis can be carried out in various media: gas phase, pure organic liquid phases or aqueous solutions.

Herein, heterogeneous photocatalysis, as represented by TiO_2, was proved to be a feasible way. Upon UV light irradiation, electron–hole (e-h) pairs can be generated in TiO_2, leading to reductive and oxidative reactions. In this way, various kinds of refractory organic pollutants can be degraded and heavy metal ions can be reduced by TiO_2 photocatalysis. A photocatalyst harnesses UV radiation from sunlight or artificial light and uses the energy to break down different substances including organic materials, organic acids, estrogens, pesticides, dyes, crude oil, microbes (including viruses) and chlorine resistant organisms, inorganic molecules such as nitrous oxides (NOx) and, in combination with precipitation or filtration, can also remove metals such as mercury. Due to this universal applicability, photocatalysis with nanoparticles as catalysts is used to reduce air pollution, in building materials, for self-cleaning surfaces in addition to water purification. Titanium dioxide (TiO_2) is the most common photocatalyst and comparably little research has been conducted on zinc oxide, ZnO, which could be a viable alternative for some applications. One of the ways to increase the efficiency of photocatalytic reaction is to couple semiconductor nanoparticles to noble metal co-catalysts to enhance the quantum yield of the electron transfer processes through improvement in charge separation in the semiconductor, discharging photogenerated electrons across the interface and providing a redox pathway with low over-potential. The interfacial charge transfer processes are influenced by the presence of a metal co-catalyst

or surface bound molecular relays. If metal nanoparticles are coupled to the semiconductor nanoparticle, then they readily accept and shuttle electrons to an acceptor molecule at the interface easily. The discharge capacity of metal nanoparticles plays an important role in dictating Fermi level equilibration between semiconductors and metal nanoparticles.

1.2. Metal-Organic Frameworks

Metal−organic frameworks (MOFs), a class of crystalline porous solids composed of metal ions/clusters and organic linkers, featuring diversified and tailorable structures as well as high surface areas, have captured widespread interest in gas sorption and separation, sensors, catalysis, etc [29]. MOFs are a class of compounds consisting of metal ions or clusters coordinated to organic ligands to form one-, two-, or three-dimensional structures. They are a subclass of coordination polymers, with the special characteristic that they are often porous. More generally, the MOF is a coordination network of organic ligands containing potential voids. A coordination network is a coordination compound extending, through repeating coordination entities, in one dimension, but with cross-links between two or more individual chains, loops, or spiro-links, or extending through repeating monomers in two or three dimensions. In certain situations, the pores are open through the removal of guest molecules (often solvents) and can be filled with other compounds. Because of this property, MOFs are of interest in the storage of gasses such as hydrogen and carbon dioxide. Many potential uses of MOFs include gas purification, gas isolation, catalysis, solids and supercapacitors [30].

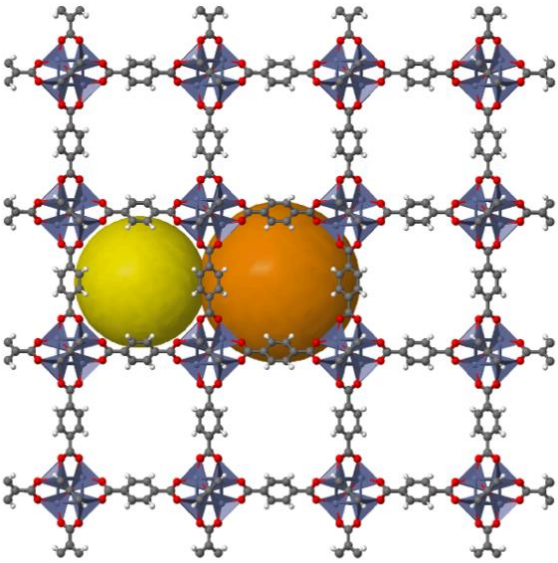

Fig. 1.2. *Metal-Organic Frameworks (HKUST)*

In MOFs, the metal ions or clusters act as centers and the ligands act as linkers or bridges. Organic ligands and metal ions are the two major components of MOFs and considered as the 'primary building units' and large aggregates formed by multidentate linkers called 'secondary building units' (SBUs) [31]. In general, a MOF is a crystalline network of a single metal ion or a metal cluster connected to multidentate organic linkers. Some of the important features of MOFs include high surface area, flexibility and low density, tunable porosity and diversity in metals and linkers. Some MOFs can even alter their pores according to external stimulus. Post synthetic modification (PSM), incorporating organic units and metal - organic complexes through reactions with linkers, has emerged as a powerful tool for changing the reactivity of pores. MOFs design can be explored to several applications from catalysis to separation and to sensing [32]. MOFs are popular in analytic fields. MOFs have been also constructed for the selective storage and separation of industrially important substances like ethylene and CO_2. They are designed for air quality control, proton conduction, solar energy and liquid phase separation applications [33]. Since the MOFs are uniform structured porous materials, it is suitable for solid-phase extraction. Some MOFs can be used directly with aqueous samples, such as the MIL (Materials of Institute Lavoisier) series, ZIF (Zeolitic Imidazolate Frameworks) series and UiO (Universitetet i Oslo) series.

During early times, MOFs were synthesized by diffusion techniques and then it is replaced by modern solvothermal methods. Other methods include grinding, electrochemical and sonochemical approaches. Slow evaporation method is conventional method used for the preparation of MOFs. This method does not require any external energy supply. The reactants are dissolved in a solvent or mixture of solvents in this method. Solubility of reagents is a major problem while preparing MOF by this method. The use of mixture of solvents can increase the solubility of reagents. Another disadvantage of this method is that it is a time consuming process.

Another synthetic method used is microwave synthetic method. This method is based on applying microwave radiation in chemical reaction. This has been widely used to synthesize crystalline MOF materials. The main advantage of microwave synthesis is its efficiency. Reduction of reaction times, phase selectivity and the control of crystal morphology are other features. The reaction time required for microwave synthesis is much faster compared to solvothermal synthetic condition [34].

The mechanochemical approach proved to be a very reliable and effective strategy for the synthesis of robust MOFs. This method is quick and having an easy procedure and it offers quantitative yields and materials of high quality also. Denovo strategy was employed for the synthesis of MOFs [31].

Since ligands in MOFs typically bind reversibly, the slow growth of crystals often allows defects to be redissolved, resulting in a material with millimeter-scale crystals and a near-equilibrium defect density. Solvothermal synthesis is useful for growing crystals suitable to structure determination, because crystals grow over the course of hours to days. However, the use of MOFs as storage materials for consumer products demands an immense scale-up of their synthesis. Scale-up of MOFs has not been widely studied, though several groups have demonstrated that microwaves can be used to nucleate MOF crystals rapidly from solution. This technique, termed "microwave-assisted solvothermal synthesis", is widely used in the zeolite literature, and produces micron-scale crystals in a matter of seconds to minutes, in yields similar to the slow growth methods.

Some MOFs, such as the mesoporous MIL-100(Fe),[35] can be obtained under mild conditions at room temperature and in green solvents (water, ethanol) through scalable synthesis methods.

A solvent-free synthesis of a range of crystalline MOFs has been described. Usually the metal acetate and the organic proligand are mixed and ground up with a ball mill. $Cu_3(BTC)_2$ can be quickly synthesised in this way in quantitative yield. In the case of $Cu_3(BTC)_2$ the morphology of the solvent free synthesised product was the same as the industrially made Basolite C300. It is thought that localised melting of the components due to the high collision energy in the ball mill may assist the reaction. The formation of acetic acid as a by-product in the reactions in the ball mill may also help in the reaction having a solvent effect in the ball mill. It has been shown that the addition of small quantites of ethanol for the mechanochemical synthesis of $Cu_3(BTC)_2$ significantly reduces the amounts of structural defects in the obtained material [36].

A recent advancement in the solvent-free preparation of MOF films and composites is their synthesis by chemical vapour deposition. This process, MOF-CVD, was first demonstrated for ZIF-8 and consist of two steps. In a first step, metal oxide precursor layers are deposited. In the second step, these precursor layers are exposed to sublimed ligand molecules, that induce a phase transformation to the MOF crystal lattice. Formation of water during this reaction plays a crucial role in directing the transformation. This process was successfully scaled up to an integrated cleanroom process, conforming to industrial microfabrication standards [37].

Stability is an important factor for the construction of MOFs. The stability of MOF refers to the chemical, thermal, hydro-thermal and mechanical stabilities. Chemical stability of MOFs can be increased by means of high valence metal ions and by the interaction between the soft ligands like triazolates, imidazolates and tetrazolates. Strong metal-nitrogen bonds are responsible for the relative stabilities of azolates. Thermal degradation occurs due to node-linker bond breakage, followed by linker combustion. Oxy-anion-terminated linkers with higher valency metal centers increases thermal stability. Hydro-thermal stability means stability in presence of moisture at elevated temperature. The presence of intermolecular or intramolecular forces, hydrophobic functional groups, prefluorinated linkers etc. with in MOF structure can increase hydro-thermal stability. Mechanical stability of MOFs is related to their porosity. The increase of porosity will decrease hydro-thermal stability. Solvent filled MOFs are found to be mechanically more stable than MOFs with empty pores. A MOF must be stable for characterization and for variable applications such as adsorption, sensing and catalysis [38].

The modular nature of MOFs and the mild conditions for their synthesis have permitted the rational structural designs of numerous MOFs and the incorporation of various functionalities by applying the concept of secondary building units (SBUs), which have well-defined geometrical shapes in the synthesis. MOFs consist of metal clusters that are joined over polytopic linkers to form finite SBUs. The different topologies of MOFs can be achieved by varying the arrangement of SBUs.

1.3. Metal-Organic Frameworks for Photocatalysis

Compared with conventional inorganic semiconductors, MOFs have been recently explored toward photocatalysis thanks to their unique advantages in following aspects: (1) the high porosity of MOFs allows the exposure/accessibility of active sites for catalysis and facilitates the transport of substrates/products; (2) the structural tunability of MOFs endows great opportunity to extend the light response over a broad range; (3) the crystalline nature with eliminated structural defects, which are usually centers of electron-hole (e-h) recombination, makes their volume recombination greatly suppressed; (4) the porous structure creates short migration paths for charge carriers prior to their reaction with substrates, thus improving the e-h separation; (5) the photosensitizer or the co-catalyst can be flexibly positioned on the framework or in the pore space, favoring the spatial separation of e-h pairs; and (6) the well-defined and tailorable MOF structures (7) ultra-high specific surface area (over 6000 m^2 g^{-1}) and rich topology and easily tunable porous structure hold great advantages in the understanding of the structure−activity relationship. Because of these merits, great efforts have been

devoted to developing MOF-based materials toward photocatalysis in recent years [29,39-41]. However, in-depth understanding of the related photocatalytic mechanisms remains limited to date. Additionally, photothermal catalysis over MOFs is at a nascent stage but exhibits important promotional effects against heterogeneous organic reactions.

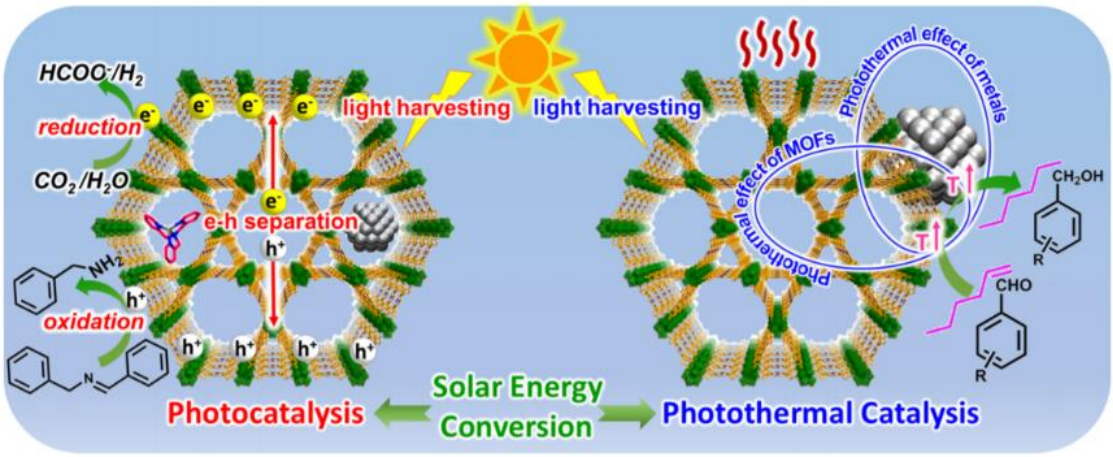

Fig. 1.3. *Schematic showing photocatalysis and photothermal catalysis promoted by MOFs*

Generally, a complete photocatalytic cycle includes light harvesting, e-h separation, and redox reactions. Typically, MOFs are able to harness sunlight with energy equal to or greater than their band edge. It is assumed that upon light irradiation, electrons are excited to the lowest unoccupied molecular orbital (LUMO) of MOFs, leaving holes in the highest occupied molecular orbital (HOMO) and generating e-h pairs. Then redox reactions take place once the charge carriers migrate to the MOF surface and meet the substrates. Though the studies of semiconductor-like behavior of MOFs have lasted for approximately 10 years, unfortunately only electron mediated metal ions/clusters were detected. The corresponding radical cations, such as excited organic linkers, have not been directly recognized. Direct evidence of both electron- and hole mediated species in MOF photocatalysts is important to unveil charge separation and semiconductor-like behavior of MOFs.

Distinct from classical inorganic semiconductors with a delocalized conduction band (CB) and valence band (VB), MOFs can be identified as molecules arranged in a crystalline lattice. In addition, some MOFs, such as MOF-5 ($Zn_4O(BDC)_3$, BDC: 1,4-benzenedicarboxylate), UiO-66 ($Zr_6O_4(OH)_4(BDC)_6$, UiO: University of Oslo) and MIL-125 ($Ti_8O_8(OH)_4(BDC)_6$, MIL: Materials Institute Lavoisier

displayed semiconductor-like behavior. Herein, the metal-oxo clusters and organic linkers can be regarded as isolated semiconductor quantum dots and light-absorbing antenna, respectively [42-44].

1.4. Zeolitic Imidazolate Frameworks (ZIFs)

Zeolitic imidazolate frameworks (ZIFs) are a group of metal-organic frameworks (MOFs) that are topologically isomorphic with zeolites. They are a sub-family of MOFs which consist of M–Im–M (where M stands for Zn, Co cation and Im stands for the imidazolate linker) formed by a self-assembly approach. ZIFs are composed of tetrahedrally-coordinated transition metal ions (e.g. Fe, Co, Cu, Zn) connected by imidazolate linkers. Since the metal-imidazole-metal angle is similar to the 145° Si-O-Si angle in zeolites, ZIFs have zeolite-like topologies [45]. Their intrinsic porous characteristics, abundant functionalities as well as exceptional thermal and chemical stabilities have led to a wide range of potential applications for various ZIF materials. Explosive research activities ranging from synthesis approaches to attractive applications of ZIFs have emerged in this rapidly developing field in recent years. A number of MOFs with zeolitic architectures have been successfully synthesised as hybrid frameworks. The diverse structures of ZIFs are similar to conventional aluminosilicate zeolites, where typically Zn^{2+} ions play the role of silicon and the imidazolate anions form bridges that mimic the role of oxygen in zeolites, with the metal–imidazole–metal (namely M–Im–M) angle of 145° [46]. As a result, ZIFs tend to form zeolite-like topologies with structures similar to those observed in zeolites. However, structures that have not been known in traditional zeolites can be also formed in ZIFs [47]. The representative ZIFs with zeolitic structures are shown in Fig. 1.5 Since these ZIFs simultaneously possess the characteristics of both MOFs and zeolites, it is not surprising that ZIFs generally display properties that combine the advantages of both zeolites and MOFs, such as ultrahigh surface areas, unimodal micropores, high crystallinities, abundant functionalities and exceptional thermal and chemical stabilities, [46,48] which make ZIFs hold great promise in many application fields including catalysis, separation and sensing. The unique characteristics of ZIFs make them different from conventional zeolites in many aspects.

ZIF-based materials have been traditionally prepared by hydrothermal or solvothermal synthesis routines in water or organic solvents respectively, with reaction temperatures varying from room temperature up to 200 °C and the reaction duration from hours to days [49].

ZIF are used in carbon capture, gas adsorption, separation of gases like hydrogen and carbon dioxide, sensing and other electronic devices, drug delivery, catalysis etc.

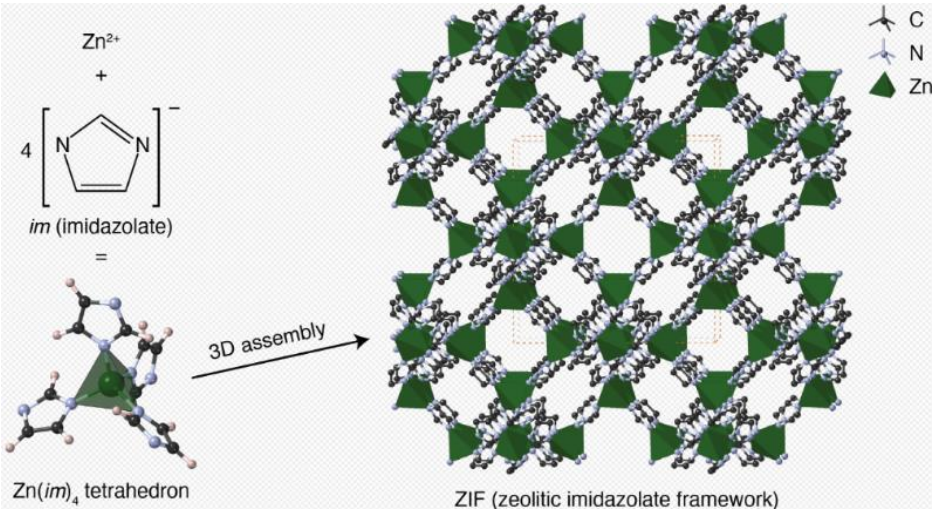

Fig.1.4. *The structure of a zeolitic imidazolate framework is made through three-dimensional assembly of metal(imidazolate)4 tetrahedra.*

1.5. Zeolitic Imidazolate Frameworks-8 (ZIF-8)

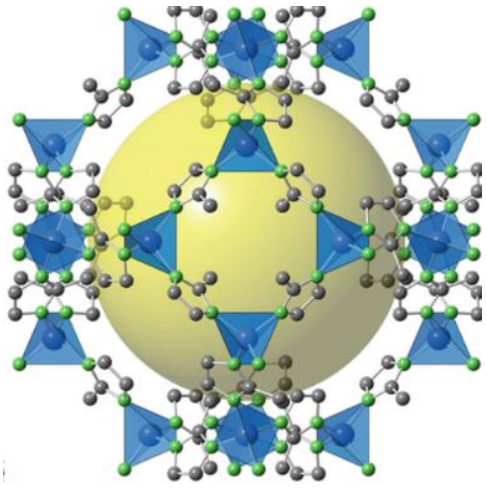

Fig.1.5. *Schematic representation of ZIF-8*

ZIF-8 belongs to the ZIF family with zinc as the noble metal. ZIF-8 possesses a microporous structure with 11.6 Å in width linking through small 3.4 Å windows. Crystallization of ZIF-8 is similar to that of zeolite, which undergoes stages of formation of saturated liquid, nucleation, and growth to form complete and stable ZIF-8 crystals. Following this process, in the first and last stages of crystallization, liquid in gel transforms from a stable form to a metastable one and finally an unstable form. Owning a weak bonding energy, unstable forms tend to assemble to a structural unit inside the crystal. In the nucleation stage, there is separation of a heterogeneous part from the saturated solution. This is considered to be the determining stage of properties, as well as the structure of the finished product. Next, molecules in the solution continue to precipitate on existed nucleation sites to form crystals. The crystals grow in a specific direction depending on different natural gel precursors. [50,51]

There have been ZIF-8 synthesis methods, like electrospinning, ultrasound, the self-template strategy, microwave, mechanochemical, dry-gel conversion, or solvothermal, that were commonly studied. In the thermal solvent method, zinc salt and 2-methylimidazole (2MI) were dissolved in different mole ratios in different solvents and were carried out in different conditions of temperature and time. Zinc salt could be $Zn(NO_3)_2.6H_2O$, $Zn(NO_3)_2.4H_2O$, $Zn(CH_3COO)_2.2H_2O$, $ZnCl_2$, or $Zn(OH)_2$. The zinc salt to 2MI molar ratio (Zn:2MI) is often taken excessively (1:4–1:6), and in some studies, the 2MI seemed to be extremely high (1:56–1:70). In several cases, Zinc is residual, but there were few studies actually using the proper reaction ratio.

Common solvents used for ZIF-8 preparation were dimethylformamide (DMF), methanol, methanol and NH_4OH, methanol and HCOONa, water, water and surfactant, or a series of solvents such as ethanol, n-propanol, 2-propanol, n-butanol, 2- butanol, n-octanol, and acetone. Generally, ZIF-8 synthesized in a less toxic solvent usually employed a largely excess amount of 2MI. Because it is a dilute reacting solution, a comparatively low yield was gained. The surfactant worked as a control agent of crystallite size (from 100–4000 nm) and morphology (from hexagon to rhombic dodecahedron). Reactions were often carried out above 100 ^oC under self-generated pressure or under 100 ^oC with stirring. Reaction time was mostly in the range of 3-6 hr or from 1-3 d [51-53].

Synthesis of ZIF-8 with particle size and crystalline morphology control is opening application opportunities in catalysis, gas adsorption and separation, as well as layered material synthesis. Much ZIF research focuses on the separation of hydrogen and carbon dioxide because a well-studied ZIF, ZIF-8, has a very high separation factor for hydrogen and carbon dioxide mixtures.

1.6. ZIF-8 for Photocatalysis

ZIF-8s are potential wide gap semiconductive materials. Thus, ZIF-8 can be considered as potential photocatalyst to degrade organic pollutants. ZIF-8 act as a photocatalyst under irradiation of UV light, mainly due to the generation of reactive charge carriers of the excited photoactive ZIF-8. Therefore, the concentration of produced ·OH radicals heavily influence the photocatalytic degradation efficiency of dyes in ZIF-8. Hence, a favourable photocatalyst in strong alkaline environment, which is completely different from other traditional photocatalysts. The terminology of HOMO–LUMO gap can be utilized to describe the photocatalytic process of ZIF-8 [54]. In the presence of UV light, there is an electron transfer from the highest occupied molecular orbital (HOMO) to the lowest unoccupied molecular orbital (LUMO) in the ZIF-8. The HOMO is mainly contributed by N 2p bonding orbitals, and the LUMO is mainly contributed by empty Zn orbitals. In general, the electrons of the excited state in the LUMO were easily lost, while the HOMO strongly demanded one electron to return to its stable state. Therefore, one electron was captured from water molecules, which was oxygenated into the ·OH active species. Then, the ·OH could decompose dye pollutants efficiently to complete the photocatalytic process.

1.7. Photocatalysis Using Polymeric Carbon Nitride

Compared to traditional photocatalysts, g-C_3N_4 exhibits high chemical stability and superior mechanical, electrical, thermal, and optical properties owing to its very high electron–hole pair transfer rate. Further, it has been found to a highly efficient photocatalyst for photoelectrochemical applications, having a narrow band gap (2.7 eV), which allows for the absorption of visible light with a wavelength of up to 450 nm. The enhanced photocatalytic efficiency was mainly attributed to the efficient retardation of the recombination of the photogenerated electron–hole pairs and the resulting increase in the lifetimes of the charge carriers. The results on this study not only confirm that the synthesized nanocomposites are highly efficient and stable photocatalysts suitable for environmental remediation, but also provide new insights into the fabrication of highly efficient ZnO-based nanocomposite materials by combining stable metal-free inorganic semiconductor photocatalysts with polymeric graphite-like carbon nitride, g-C_3N_4. PCN (polymeric carbon nitride), a nonmetallic layered semiconductor, has gained wide research interest as photocatalyst over recent years [56]. g-C_3N_4 is studied as a new-

generation photocatalyst to recover the photocatalytic activity of traditional photocatalysts like TiO_2, ZnO, and WO_3.

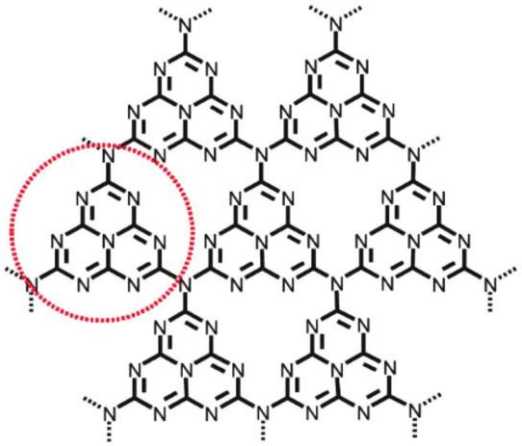

Fig. 1.6. *Polymeric Carbon Nitride*

Graphitic carbon nitride (g-C_3N_4) is assumed to have a tri-s-triazine nucleus with a 2D structure of nitrogen heteroatom substituted graphite framework which include p-conjugated graphitic planes and sp^2 hybridization of carbon and nitrogen atoms. Bulky carbon nitride can be synthesized through thermal condensation of nitrogen-rich (without a direct C-C bound) precursors such as cyanamide, dicyandiamide, thiourea, urea, and melamine. Also, it can be synthesised through polymerization of nitrogen-rich and oxygen-free precursors (comprising the pre-bonded C-N core structure) by physical vapour deposition, chemical vapour deposition, solvothermal method, and solid-state reactions. Having the band gap of 2.7 eV and the conduction and valence band position at −1.4eV and 1.3 eV, respectively, versus NHE (normal hydrogen electrode), g-C_3N_4 have shown great ability to carry photocatalytic activity in the visible light irradiation without the addition of any noble-metal co-catalyst. Apart from visible light utilization, bulky carbon nitride is hampered by high-charge carrier recombination which reduces its photocatalytic activity. Different researchers have studied on the modification of g-C_3N_4 to counteract the challenge of charge carrier recombination and band engineering. Several modifications have been studied over decades including structural modification, doping, modification with carbonaceous and plasmonic material, and heterojunction composite formation. Changing the morphology of the synthesized photocatalysts plays a significant effect in its photocatalytic activity Optical, electronic, mechanical, magnetic, and chemical properties of carbon nitride materials are highly dependants on the change of size, composition, dimension, and shape. Hard and soft templating methods, template-free methods, and exfoliation strategies are among the methods used to modify the

structure of the synthesized carbon nitride photocatalysts. Templating modifies the physical properties of carbon nitride semiconductor materials by varying morphology and introducing porosity. Template-free method creates vacancies in carbon nitride photocatalysts resulting to introduction of additional energy levels or acting as reactive sites, and thus profoundly changing the overall photocatalytic activity. Exfoliation modifies the bulky carbon nitride into nano-sheet carbon nitrides which increase the surface area for active sites, hence increasing its photocatalytic activity [56,57]. Also, carbon nitride can be modified into nano-rods and nanotubes which all have effects on the photocatalytic activity of the synthesised photocatalysis. One and the most popular modification of a single semiconductor is the metal/non-metal doping and surface modification forming metal/semiconductor-heterostructured photocatalysts. Different researchers have studied doping g-C_3N_4 with different metals or non-metals for band gap engineering and overcoming the challenge of charge carrier (electrons-holes pair) recombination. Yan et al. reported the study on the impact of doped metal (Na, K, Ca, and Mg) on g-C_3N_4 for the photocatalytic degradation of enrofloxacin (ENR), tetracycline (TCN), and sulfamethoxazole (SMX) as representatives of common antibiotics under visible light irradiation. In their study, it was observed that in all the degradation of three representative antibiotics the degradation activity followed the same sequence of g-CN-K>g-CN-Na>g-CN-Mg>g-CN-Ca>g-CN. This was attributed by the decreased band gap of doped g-C_3N_4 from 2.57 to 2.29–2.46 eV as a result of a red shift caused by the doped metal resulting to an extended visible light response and high-charge carrier separation of the as-prepared photocatalytic semiconductor, hence increasing the production of ·OH reactive species. In the study done by Xu et.al, it was also evident that doping Fe on the surface-alkalinized g-C_3N_4 reduced the recombination of photo generated charge carriers (electron and holes) and the band energy of which lead to high photocatalytic activity of the doped g-C_3N_4 on the degradation of tetracycline under visible light ($\lambda \geq 420$) irradiation. Jiang et.al synthesized the nitrogen (N) self-doped g-C_3N_4 nano sheets with tunable band structures for enhanced photocatalytic tetracycline degradation in the visible light irradiation. It was evidently proved that doping nitrogen (N) on g-C_3N_4 nanosheets increased the semiconductor photocatalytic activity as a result of reduced charge recombination as proved by the photoluminescence (PL) emission spectra study. Ling et al. reported the study of the synergistic effect of non-metal (sulphur) doping on the photocatalytic property of g-C_3N_4 using the first-principle calculations. The obtained results indicated narrowing of the band gap and increased visible light response on S-doped g-C_3N_4 photocatalyst. The effect of metal or non-metal doping on g-C_3N_4 was also revealed in studies done by Guo et al. who used potassium (K) and iron (Fe),

Fan et al. who used manganese (Mn), Xie et al., Zhu et al., and Wu et al. who used cobalt (Co). Shu et al. using sodium (Na) synthesized doped mesoporous g-C_3N_4 nanosheets for photocatalytic hydrogen production of which the results showed that the doped nanosheets exhibited lower recombination of photogenerated charge carrier (electron–hole pairs) than bulk g-C_3N_4, hence resulting to excellent visible light photocatalytic hydrogen evolution efficiency up to about 13 times that of bulk g-C_3N_4. All these prove that doping g-C_3N_4 with metal ion or non-metal has a significant improvement on the photocatalytic efficiency in the visible light irradiation [56-58].

1.8. ZnO with Polymeric Carbon Nitride

Among the semiconductors used for the photocatalytic degradation, zinc oxide (ZnO) has been proved to be one of the best photocatalysts because of its non-toxicity, high efficiency and strong oxidative ability. Owing to its wide band gap (3.37 eV), ZnO can only absorb the UV light ($\lambda < 368$ nm), which accounts for less than 5% of the solar energy [55]. Moreover, the recombination rate of photo-induced electron–hole pair of ZnO also stayed at a very high level. Thus, the practical application of the pure ZnO photocatalyst is seriously impeded. Hence, numerous investigations have been made to design ZnO-based composite photocatalyst with high visible light activity. graphite-like carbon nitride (g-C_3N_4) has attracted much attention for its chemical inertness, low density, cheap and wide range of light absorption. Limited by its inherent low quantum efficiency and high recombination rate of electron-hole paris, the photocatalytic efficiency of g-C_3N_4 was low. when it is combined with another semiconductor like ZnO, to construct heterojunction g-C_3N_4/ZnO, which can restrain the recombination of photogenerated electron-holes the photocatalytic activity improves a lot. ZnO coupled with g-C_3N_4 has been proven to have remarkable photocatalytic performance due to the efficiency separation of charge carriers. provide a large interfacial area to obtain the rapid charge separation and consequently increase the carrier separation efficiency. And the g-C_3N_4/ZnO could also enhance the carrier separation efficiency and extend the range of light absorption. This combination is favorable to the mass transfer reaction of active substances in the process of photocatalysis.

1.9. ZIF-8 Derived ZnO with Polymeric Carbon Nitride

The MOF/metal oxide composites are usually prepared either from self-assembling MOFs onto the surface of previously prepared metal oxide nanoparticles, rods, or wires or via the formation of a metal oxide in/on previously formed MOFs. However, these methods require two steps and lead to substantial

energy consumption during synthesis. Therefore, a one-step synthesis of MOF/metal oxide directly from metal salts is highly advantageous. ZIF-8 with zeolite microporous structure is a type of MOFs formed by the coordination of Zn^{2+} and 2-methylimidazole (2-MI), which can be used as a photocatalyst to degrade organic pollutants. Rotation of imidazolate linkers makes ZIFs more flexible and more susceptible to structural transitions induced by uptake of guest molecules, leading to the rapid development of MOF-based materials. Transition metal element, have been extensively studied in the heterogeneous catalytic reaction. If a tetrahedrally coordinated metal is used then, they could coordinate by nitrogen atoms in the 1, 3-positions of benzimidazolate linkers forming a tetrahedral building unit, ZIF (Zeolitic imidazolate frameworks) could be built accordingly. In addition, rotation of imidazolate linkers makes ZIFs more flexible and more susceptible to structural transitions induced by uptake of guest molecules, leading to the rapid development of MOF-based materials. PCN photocatalyst and ZIF photocatalyst mainly consist of large size pores, and both of them show an alike curve. However, with the combination of the two, the pores size of the formed complex had been reduced The modified structure is more beneficial to the photocatalytic reaction. And the fastest electron movement rate, which was certainly indicated that a suitable co-catalyst could provide sufficient orbit for electron transport.

The synergistic effect of ZnO and ZIF-8 lead to the extra photocatalytic ability. ZnO/ZIF-8 photocatalyst shows high photostability. ZIF is good due to its high specific surface area, uniform channels, and regular pores. the band gap of ZIF-8 is about 4.9 eV, compared to the traditional semi-conductive photocatalysts (e.g., ZnO, SnO and TiO_2), ZIF-8 can only be motivated by a photoelectron containing higher energy. Thus, hybridizing ZIF-8 with other semiconductors can be an efficient way to improve its photocatalytic properties. To date, several semiconductor-ZIF-8 hybrid photocatalysts have been synthesized, such as TiO_2/ZIF-8, Zn_2GeO_4/ZIF-8, and ZnO/ZIF-8. They show higher potential for improvement of photocatalytic activity as compared to single catalysts. In recent years, ZnO/ZIF-8 hybrid photocatalysts have drawn much attention and have been widely studied due to their advantages of nontoxicity, thermal and chemical stability and high photocatalytic activity. This hybrid exhibits a size selective photocatalysis due to selective adsorption and permeation effect of ZIF-ZnO effects. It exhibited superior capability in adsorption and degradation under UV irradiation, which can be used as a potential photocatalyst.The properties and structures of ZnO/ZIF-8 hybrid photocatalysts can be well controlled by the method of synthesis. ZIF-8 derived ZnO with polymeric Carbon Nitride can be used for photocatalytic derived pollutant degradation, water splitting for Hydrogen production, and CO_2 reduction [56,58,59].

1.10. Dyes

A dye is a coloured substance that chemically bonds to the substrate to which it is being applied. This distinguishes dyes from pigments which do not chemically bind to the material they colour. The dye is generally applied in an aqueous solution, and may require a mordant to improve the fastness of the dye on the fiber. There are a variety of different coloring dyes depending on their use. Examples of dye groups include reactive dyes, disperse dyes, direct dyes, vat dyes, sulphur dyes, anthraquinone dyes, cationic azo dyes, cationic methine dyes, solvent dyes, acid dyes, metal complex dyes, naphthoquinone and benzoquinone dyes. By definition, dyes can be said to be coloured, ionizing and aromatic organic compounds which show an affinity towards the substrate to which it is being applied. It is generally applied in aqueous solution. Discharge of dyeing industry wastewater into natural water bodies is not desirable as the colour prevents re-oxygenation. Many dyes are difficult to degrade, as they are resistant to aerobic digestion. Dyes can also cause allergic dermatitis and skin irritation. Some of them have been reported to be carcinogenic and mutagenic. There are a lot of physical and chemical techniques such as coagulation, ozonization, membrane filtration, electrolysis; oxidation, active sludge biochemical processes, bio-degradation etc. has been widely used for the removal of dyes from wastewater.

Among them, the heterogeneous photocatalytic method is an authentic technique that can be used effectively to oxidize the organic contaminants in the water system. Semiconductors are the key materials in the process, in which zinc takes a role model. Almost complete mineralization of organic compounds to carbon dioxide, water and inorganic anions have taken place.

1.10.1. Rhodamine B (Rh B)

Rhodamine B is an amphoteric dye that belongs to the family of Xanthene dyes. Rhodamine B can be used to dye silk, cotton, wool, fibers, nylon, acetate fibers, paper, spirit inks and lacquers, soap, wood stains, feathers, leather and distempers on china clay etc. It has also been used as a drug and cosmetic colour in aqueous drug solutions, tablets, capsules, toothpaste etc. It is often used as a tracer dye within water to determine the rate and direction of flow and transport. Pollution of water due to the discharge of effluents from dyeing industries affects the environment due to its toxicity.

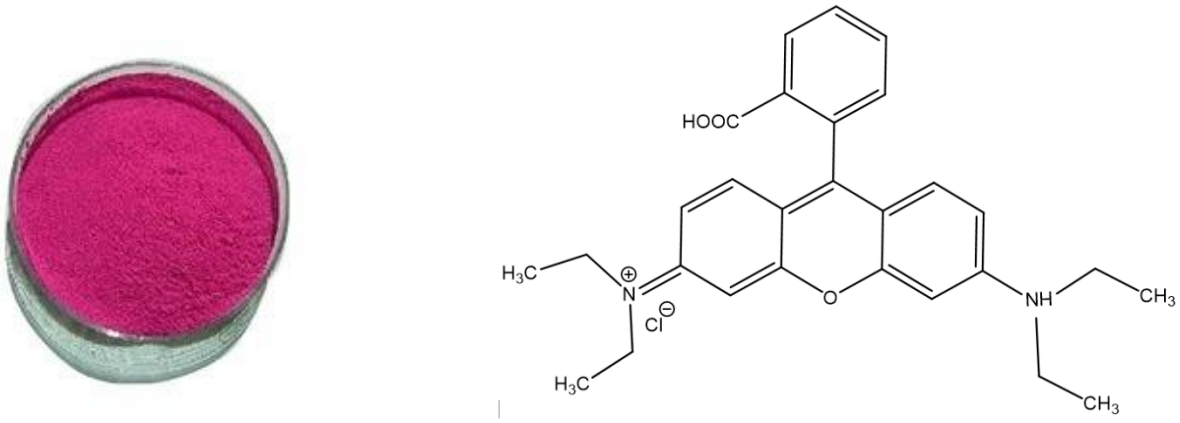

Fig. 1.7. *Rhodamine B dye and its structure*

1.11. Literature Review

Recently, stable and metal free organic graphitic carbon nitride (g-C_3N_4) semiconductor is reported as one of the active visible light photocatalytic materials (Wen et al., 2016; Martha etal., 2013; Patnaik et al., 2016). The g-C_3N_4 possessing π-conjugated electronic structure with the band gap of about 2.7 eV (Zhang et al., 2013), shows superior thermal, chemical, mechanical, electrical and optical properties (Huang et al., 2013). Further the g-C_3N_4/ZnO nanocomposites, synthesized with various concentration of g-C_3N_4 and ZnO are proved to be the potential candidates to enhance the efficiency of photocatalytic activity under visible light irradiation. The ZnO/g-C_3N_4 nanocomposites synthesized by microwave method showed photocatalytic degradation of ~98% in a time period of 80 min against Rhodamine B (RhB) dye under visible light (Osman et al., 2017). The g-C_3N_4/ZnO composite photocatalysts synthesized with various weight percent of ZnO by a simple calcination process increased the photodegradation efficiency of methyl orange about to 3 times under visible light irradiation and *p*-nitrophenol to about 6 times as compared with that of pure g-C_3N_4 (Jia-Xin Sun et al., 2012). The ZnO/g-C_3N_4 nanocomposite heterostructures prepared by reflux method exhibited 99% of photocatalytic activity in a time period of 140 min against methylene blue under the illumination of visible light as compared to that of pure g-C_3N_4 (Fageria et al., 2015). Thus the previous reports evidently show that the g-C_3N_4/ZnO binary nanocomposites acquired relatively high photocatalytic activity.

Previous reports suggest that enhancement in the (002) polar facets of ZnO nanoparticles provide high surface area and favors to improve the photocatalytic activity (Zeng et al., 2009; Wang et al., 2011). The XRD analysis reveals that the ZC6 binary and ZC6G30 ternary nanocomposite possess relatively enhancement in (002) polar plane which can be expected to enhance the dye degradation efficiency of the nanocomposites under the visible light irradiation.

Fourier transform infrared (FT-IR) spectra of ZnO, ZC6 binary and ZC6G30 ternary nanocomposites were recorded in the range of 400-4000 cm^{-1}. The frequency observed at 559 cm^{-1} corresponds to Zn-O bending vibrations (Wan et al., 2015). In the ZC6 binary ZC6G30 ternary nanocomposites the peak observed at ~805 cm^{-1} is assigned to the s-triazine ring of g-C_3N_4 which indicates the intense interaction between ZnO and g-C_3N_4 (Liu etal., 2011; Wan et al., 2015). The several bands observed in the range of 650-1200 cm-1 are attributed to g-C_3N_4 (Liu et al., 2008). The band appeared at 1240 cm^{-1} in ZC6G30 ternary nanocomposite is assigned to aromatic C-N stretching (Liu et al., 2008; Zhu et al., 2014). The bands at 1432 cm^{-1}, 1561 cm^{-1} and 1630 cm^{-1} are assigned to typical stretching vibrational modes of heptazine-derived repeating units (Li et al., 2014). The broad band obtained around 3000-3500 cm^{-1} is assigned to the hydroxyl group of H_2O as well as to the –NH moieties (Wan et al., 2012; Zhu et al., 2014). Thus in the present investigation the FT-IR spectral analysis confirms the formation of binary and ternary nanocomposites. However, the excess amount of g-C_3N_4 above the optimal value of 6 wt.% in the binary nanocomposites acts as electron-hole pair recombination centre and decreases the photocatalytic activity (Yuan et al., 2016).

Under the visible light irradiation ZC6G30 ternary nanocomposite excites the electrons from VB of g-C_3N_4 to its CB and the electrons migrate to the CB of ZnO and then migrate to the GO, as the work function of GO (-0.08 eV vs normal hydrogen electrode) is lower than that of the ZnO (Dai et al., 2015).

2. CHARACTERIZATION TECHNIQUES

The following instruments were used in the characterization of the compounds

2.1. Fourier Transform Infrared Spectroscopy (FT-IR)

FT-IR (Fourier Transform Infrared) is a method of obtaining a spectrum by applying the Fourier Transform (FT) for an interferogram, which is by first obtaining the infrared spectra of a sample using an interferometer (Figure 2.1).

Principle

The total energy of a molecule is the sum of the rotational, vibrational, and electronic energy levels according to the Frank-Condon theory. Interaction between the EM radiation and molecular motions occurs in the IR field. So the molecule absorbs the appropriate wavelength and is excited to the level of higher vibrational energy. The absorbed radiation frequencies are determined through an IR spectrometer. The resulting diagram of the material's absorbed energy vs frequency is called the IR continuum. Different materials have different vibrations and produce different IR spectra, which can be used to classify a substance. A functional group or atom's vibrational frequency can correspond with the frequency of the absorbed IR radiations. The IR stretching frequency of two bonded atoms can determined by the equation:

$$\vartheta = (1/2\pi)(\sqrt{k/\mu})$$

$$\mu = m_1 m_2 / (m1 + m2)$$

Where, υ = frequency in Hz, k = force constant, μ = reduced mass,

Instrumentation and working

There are two types of IR instrumentation: dispersive and non-dispersive. The dispersive instruments use dispersive spectrometers on a prism or grating. And the non-dispersive type uses interference filters, tunable source laser, or an interferometer. The interferometer serves as the coherent source of light, and the radiation will pass through the beam splitter. The divided radiation is deviated and one goes as undeflected and at 900 the other is focused. From this the divided beams interact respectively with a

fixed and a moving mirror and return to the beam splitter again and a combined beam is produced it is then transformed as an interferogram.

a b

Fig. 2.1. *a) a FT-IR instrument. b) schematic diagram of FTIR*

In the present study, Fourier Transform Infrared (FT-IR) spectra were recorded by Perkin Elmer FT-IR / FIR Spectrometer, Frontier using KBr as a reference.

2.2. X-Ray Diffraction Spectroscopy (XRD)

X-ray powder diffraction analysis (XRD) is perhaps the most widely used X-ray based analytical techniques for characterizing materials. As the name suggests, the sample is usually in a powdery form, consisting of fine grains of crystalline material to be studied. The term 'powder' really means that the crystalline domains are randomly oriented in the sample. Therefore, when the 2-D diffraction pattern is recorded, it shows concentric rings of scattering peaks corresponding to the various d spacings in the crystal lattice. The positions and the intensities of the peaks are used for identifying the underlying structure (or phase) of the material. For example, the diffraction lines of graphite would be different from diamond even though they both are made of carbon atoms. This phase identification is important because the material properties are highly dependent on structure.

Principle

The three-dimensional structure of crystalline materials, such as minerals, is defined by regular, repeating planes of atoms that form a crystal lattice. When a focused X-ray beam interacts with these planes of atoms, part of the beam is transmitted, part is absorbed by the sample, part is refracted and scattered, and part is diffracted. Diffraction of an X-ray beam by a crystalline solid is analogous to diffraction of light by droplets of water, producing the familiar rainbow. X-rays are diffracted by each mineral differently, depending on what atoms make up the crystal lattice and how these atoms are arranged. When an X-ray beam hits a sample and is diffracted, we can measure the distances between the planes of the atoms that constitute the sample by applying Bragg's Law, named after William Lawrence Bragg, who first proposed it in 1921.

Bragg's Law is,

$$n\lambda = 2d \sin\theta$$

Where the integer 'n' is the order of the diffracted beam, 'λ' is the wavelength of the incident X-ray beam, 'd' is the distance between adjacent planes of atoms (the d-spacing), and 'θ' is the angle of incidence of the X-ray beam. Since we know 'λ' and 'θ', we can calculate the d- spacing.

The Scherer equation, in X-ray diffraction and crystallography, is a formula that relates the size of sub-micrometer particles, or crystallites, in a solid to the broadening of a peak in diffraction pattern. Scherer equation is limited to nano-scale particles. The particle size of the prepared samples were determined by using Scherer's equation as follows:

$$D \approx 0.9\lambda / \beta \cos\theta$$

Where 'D' is the crystal size, 'λ' is the wavelength of X-ray, 'θ' is the Braggs angle in radians and 'β' is the full width at half maximum of the peak in radians

Instrumentation and working

In X-ray powder diffractometry, X-rays are generated within a sealed tube that is under vacuum. A current is applied that heats a filament within the tube; the higher the current the greater the number of electrons emitted from the filament. This generation of electrons is analogous to the production of electrons in a television picture tube. A high voltage, typically 15-60 kilovolts, is applied within the

tube. This high voltage accelerates the electrons, which then hit a target, commonly made of copper. When these electrons hit the target, X-rays are produced. The wavelength of these X-rays is characteristic of that target. These X-rays are collimated and directed onto the sample, which has been ground to a fine powder (typically to produce particle sizes of less than 10 microns). A detector detects the X-ray signal; the signal is then processed either by a microprocessor or electronically, converting the signal to a count rate. Changing the angle between the X-ray source, the sample, and the detector at a controlled rate between preset limits is an X-ray scan.

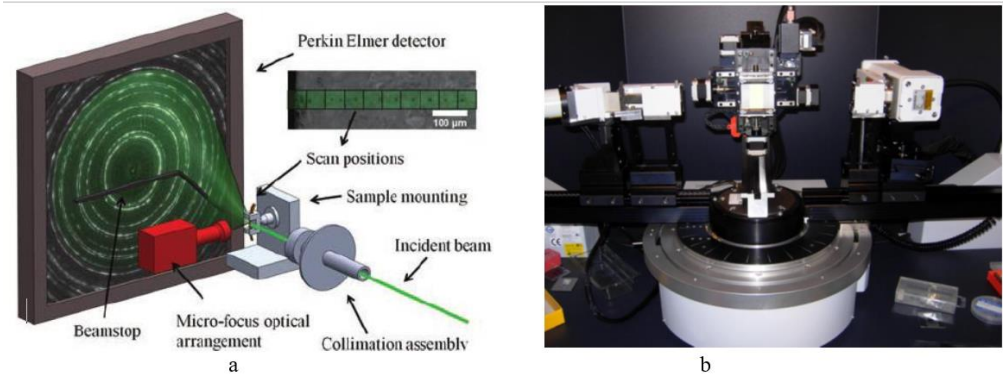

Fig.2.2. *a) Schematic diagram of X-Ray Diffractometer b) Typical X-Ray Diffractometer*

2.3. UV-Visible spectroscopy (UV-VIS)

UV-Visible spectroscopy is a type of spectroscopic technique used to analyze a sample's concentration and to classify the sample's functional groups. This technique extends to both liquid- and solid-state samples. In UV-Vis spectroscopy the interaction of matter with the UV-Visible light wavelength is measured. The visible region ranges from 800-400 nm and UV region is 400-200 nm

Principle

The basic principle of UV-Vis spectroscopy is the Beer-Lambert law, which states that: when a beam of monochromatic light is passed through a solution of an absorbing substance, the rate of decrease of intensity of radiation with thickness of the absorbing solution is proportional to the incident radiation as well as the concentration of the solution.

The expression of Beer-Lambert law is

$$A = \log (I_0/I) = \varepsilon cl$$

Where, ‘A’ is the absorbance, ‘I_0’ is the intensity of light incident upon sample cell, ‘I’ is the intensity of light leaving sample cell, ‘C’ is the molar concentration of solute, ‘L’ is the length of sample cell (cm), ‘ε’is the molar absorptivity.

Instrumentation and working

Tungsten filament lamp and deuterium arc lamps are the widely used light source for UV-area. Xenon lamp is used as source of visible light in the field. Double beam spectrophotometers are used in the research. This consists of a light source which is monochromator; the light is separated into two beams using mirrors. One beam passes through the sample, and the other passes through the reference. It is important that both the reference and the sample should be transparent, so that it passes through the light incident. For comparable quartz cuvettes or fused silica the sample and comparison must be taken. The detectors detect and measure the intensity of transmitted light, and the recorders record the data. Double beamed instrument comprises two detectors. This is useful for calculating reference beam and sample simultaneously. The intensity of the sample beam is taken as 'I' and that of reference is 'I_0' since the reference beam experienced no light absorption. On the spectrometer the scanning is performed automatically.

Fig. 2.3.1. *UV instrument*

Differential Reflectance Spectroscopy (DRS)

In the case of granular/powder or thin films of high surface roughness, the reflection is not specular (although for each incident photon, the reflection is specular), and hence we cannot measure the transmitted intensity (it is too low) to get the absorption of the sample as in case of specular case. Therefore, for powders or thin films of high surface roughness, we use DRS where apart from recording reflectance, we can also measure absorbance of the sample collecting all the diffuses reflected beams (from the sample surface) using a semispherical collector.

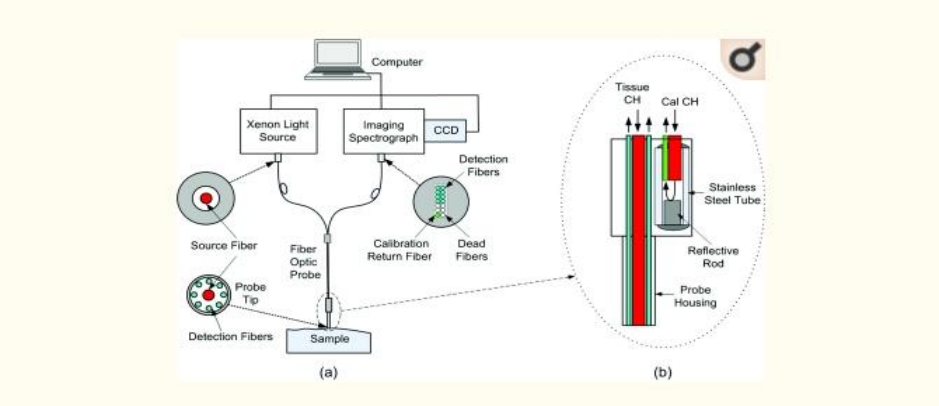

Fig. 2.3.2. *Schematic diagram of UV-VIS DRS System*

(DRS) is a surface analytical technique. It uses ultraviolet (UV), visible, or infrared (IR) light as a probing medium. The interaction of light with "strongly absorbing materials", such as metals, alloys, semiconductors, etc. occurs in the first 10–20 nm. Thus the differential reflectometer probes 50–100 atomic layers into nontransparent solid surfaces. Because of the specific probing depth of light, DRS fills the gap between other surface techniques such as ion-scattering, Auger spectroscopy, and ESCA (electron spectroscopy for chemical analysis), which probe 1, 5, or even 20 monolayers, and X-ray diffraction (XRD) which probes as deep as 1–50 μm into a bulk material. The information gained by DRS is somewhat different from that obtained by the other surface techniques mentioned. A "differential reflectogram" reveals details about the electron structure around the Fermi surface. Specifically, the instrument allows the exact measurement of the energies which electrons absorb from photons as they are raised into a higher, allowed energy states. Since each material has a specific electron-band structure the measurement of the characteristic energies for electron "interband transitions" serves as a means for identifying these materials. The application of DRS is, of course, not restricted to strongly absorbing materials such as metals, alloys, or semiconductors. Its strength has likewise been demonstrated in the

identification and characterization of transparent or semitransparent surface layers as observed in thin-film corrosion products on metal substrates. DRS is used to scan two samples whose properties differ slightly. Thus, the main advantage of DRS over conventional optical techniques lies in its ability to eliminate any undesirable influences of oxides, windows, electrolytes, instrumental variations, and the like, owing to the differential nature of the technique. No vacuum is needed unless measurements in the vacuum UV are desired. Thus, the formation of a surface layer due to environmental interactions can be studied in situ. The measurements are fast: a complete differential reflectogram, that is, an automatic scan from the UV through the visible into the IR region, is accomplished in about 3 min.

2.4. Photoluminescence Spectrometer (PL)

Photoluminescence spectroscopy (PL spectra) is a contactless, non-destructive method of studying the materials' electronic structure. In Photoluminescence spectroscopy, a light beam is exposed to a sample incident, then it is excited to a higher energy state by absorbing energy from the event beam, which means that the sample has an excess energy. Through the emission of light, the sample dissipates this excess energy and this effect is known as photoluminescence. Photoluminescence spectroscopy is used to detect a sample's defects, band difference, impurity levels and recombination mechanism.

Principle

Photoexcitation allows electrons to migrate within the material into activated, energized states. Once these electrons return to their equilibrium state, they discharge the excess energy and either cause light emission (a radiative procedure) or not (a non-radiative procedure). The energy of the emitted light (photoluminescence) is proportional to the difference in energy between the two energy states in which the transfer of electrons takes place. The most commonly recognized radiative difference in semiconductor systems is in the conductive and valence bands between the states, this energy disparity being known as bandgap. Laser light generates excitation with a much greater intensity than the optical band gap for an analyser of PL spectroscopy. The excited photo carriers are made up of electrons and holes that relax towards their unique edges of the band and recombine by transmitting light at the band gap. Radiative transitions to semiconductors can be due to small deformities or impurities. Analysis of the PL spectra helps detect defects or contaminations. The specific rates of radiative and non-radioactive recombination can be determined by a detailed study of the temperature range. Non-radioactive recombination is performed at higher temperatures, and the PL rate decreases exponentially. In the sense

that the spectrum of absorption measures the transition from ground to excited state, where PL performs the transition from excited state to ground state, PL is not exactly the same as the spectrum of absorption. The amount of time between absorption and emission is usually extremely short. The excitation spectrum is a plot of intensity of the emission versus wavelength of excitation. The wavelength at which the molecule absorbs energy is the excitation wavelength.

Instrumentation and Working

The block diagram and the major components of the instrument that is used to measure photoluminescence are shown in Fig. 2.4. Electromagnetic radiation from an ultraviolet - visible source passes through a wavelength selector and through the cell as in a spectrophotometer. Of the several sources of incident radiation that have been used for photoluminescence measurements, the mercury - arc lamp and the 150W xenon gas discharge lamp have been used most often. Because the mercury - arc lamp emits line spectra rather than a continuum, it cannot be used in instruments in which the wavelength of the incident radiation is scanned. Unlike the measurement of absorption in a spectrophotometer, however, a portion of the emitted radiation that exists from the cell is measured. Because the luminescent radiation can be emitted in broad bands that are centered at different wavelengths, a second wavelength selector is required in the path of the emitted radiation between the cell and the detector. Fig. 2.4.a. Block diagram of the Fluorescence Spectrophotometer. The emitted radiation is not usually measured in line with the exciting radiation as in absorptive measurements, owing to possible spectral interference from the exciting radiation. Photoluminescence has been measured at many angles relative to the incident radiation and at many locations within the cell. The most common practice is to measure the emitted radiation at 90°C from the path of the exciting radiation and at the center of the cell. The signal from the detector is amplified, if required and routed to a read out device.

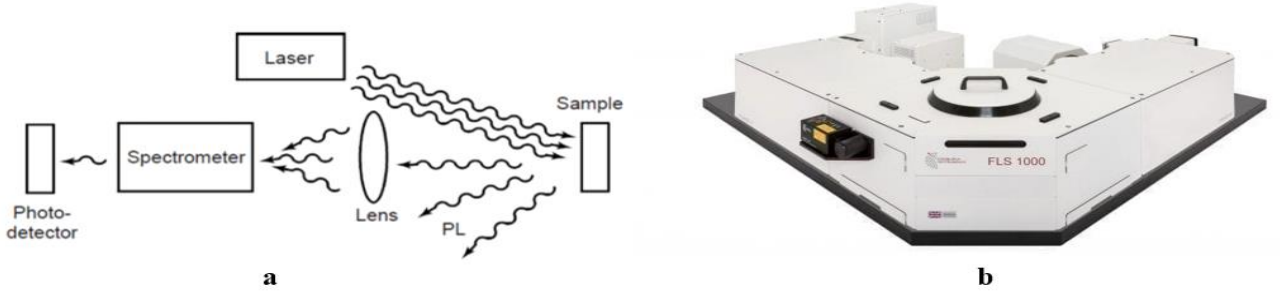

Fig. 2.4. *a) schematic diagram of instrumentation b) PL instrument*

3. EXPERIMENTAL SECTION

3.1. Materials

Urea (99%, Merck Life Science Pvt. Lmtd.), $Zn(NO_3)_2.6H_2O$ (99%, Sigma Aldrich), 2-methylimidazole (97%, HiMedia Laboratories), Hydrogen Peroxide (30%, Merck Life Science), Methanol (99.8%, Sigma Aldrich).

3.2. Preparation of g-C_3N_4 (CN)

Graphene-like porous g-C_3N_4 nanosheets were synthesized via direct pyrolysis of thiourea followed by a thermal exfoliation. About a half crucible of urea is pyrolysed at 530 ^{0}C for 3 hr at a heating rate 3^0 C/min and is kept at 530 ^{0}C for 1 hr. And allowed to cool to room temperature to obtain bulk g-C_3N_4.

3.3. Preparation of g-C_3N_4 (CN) nano sheets

The obtained bulk g-C_3N_4 is calcinated at 530 ^{o}C for 3hrs at a heating rate 3^0 C/min and again heated at 530 ^{o}C for 1hr to obtain g-C_3N_4 nano sheets.

3.4. Preparation of ZIF-8 and ZnO

1.6422 g of 2-methylimidazole (2MI) was absolutely dissolved in 50 mL methanol and then slowly poured into another 50 mL methanol containing 1.4874 g $Zn(NO_3)_2.6H_2O$ after sonicating both for 5 min separately. The solution was stirred for 3hrs and then kept standing at room temperature. After 24 h crystallizing, it was centrifuged and washed with 15 mL of methanol and then dried at 80 ^{0}C for 12hrs to obtain ZIF-8 [60]. The prepared ZIF-8 was heated at 600 ^{0}C for 5 hr at a heating rate of 2 ^{0}C/min to obtain ZnO.

3.5. Preparation of ZnO@g-C_3N_4 (ZCN) Composites

5 mg of g-C_3N_4 nano sheet is taken in 15 mL of methanol and sonicated for about 30 min. Then 95 mg of ZIF-8 derived ZnO is taken in 15 mL of methanol and sonicated for 10 min and added to the g-C_3N_4 in methanol, drop by drop and stirred for 1 hr. Then mixture is transferred into a hydrothermal bomb and is heated to 120 ^{0}C for 12 hrs. After cooling to room temperature it is centrifuged and washed with

10 mL of ethanol and dried at 80 ^{0}C for 12hrs in an air oven. The obtained sample is marked as ZCN 5 which contain 5% g-C_3N_4 nano sheets.

3.6. Preparation of Dye Solution

10 ppm dye solution was prepared by dissolving 10 mg of Rhodamine B in 1L of water. This prepared dye solution was used for further degradation study using the prepared nano-photocatalyst.

3.7. Preparation of initiator

About 0.250 mL of 30% H_2O_2 is taken and made upto 100 mL.

3.8. Evaluation of Photocatalytic Activity

Photocatalytic activities of the samples were evaluated by the photocatalytic degradation of Rhodamine B (RhB). Typically, 25 mg of the photocatalyst was dispersed in 50 mL of 10 ppm Rh B aqueous solutions in a beaker. The reaction system was magnetically stirred in dark for 1 h to ensure the establishment of an adsorption/desorption equilibrium between the photocatalyst and RhB and then the suspension was exposed to natural sunlight. At given time intervals, about 3 mL aliquots from each sample were taken, followed by centrifugation and filtration to remove the photocatalyst. The concentration of the clean transparent solution was determined by measuring the absorbance of RhB at 554 nm using a spectrophotometer (2600 Shimadzu UV-visible spectrophotometer). The percentage of degradation is reported as C/C_0, where ‘C’ is the absorption of the dye solutions taken at each interval at maximum absorption peak, and ‘C_0’ is the absorption of the initial concentration when the adsorption-desorption equilibrium is reached.

4. RESULT AND DISCUSSION

4.1. X- Ray Diffraction analysis

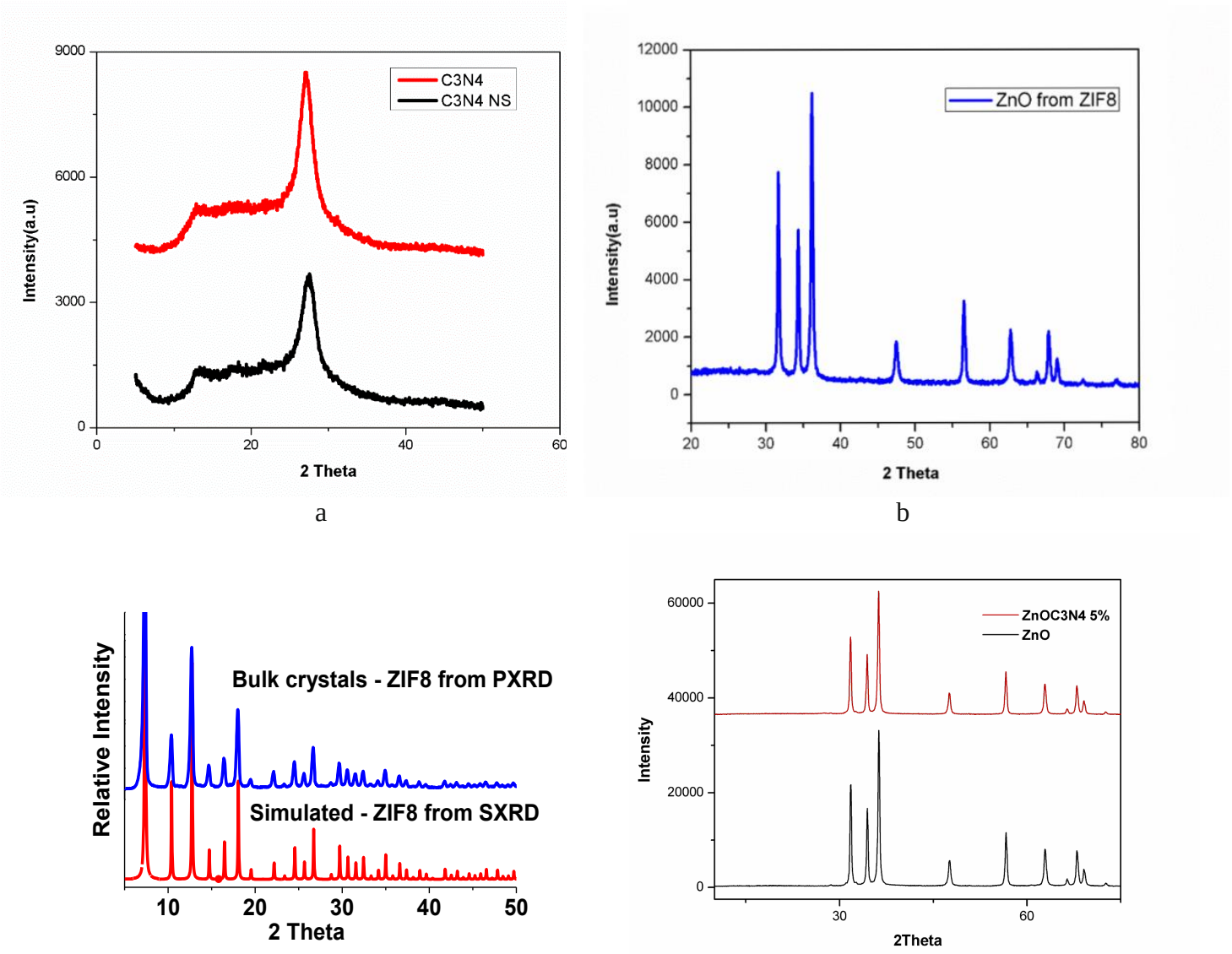

Fig. 4.1. *XRD patterns of g-C3N4 bulk and nanosheet, ZIF-8, ZnO from ZIF-8, and ZCN 5*

These figures show the XRD patterns of g-C_3N_4 bulk and nanosheet, ZIF-8, ZnO from ZIF-8, and ZCN 5. A strong peak at 27.5°, corresponding to the characteristic diffraction peak (002) of g-C_3N_4 [67] can be also observed. The main characteristic peaks can be indexed as the hexagonal ZnO with wurtzite

structure. The presence of strong peaks at 2θ = 7.30°, 10.35°, 12.70°, 14.80°, 16.40° and 18.00° correspond to planes (110), (200), (211), (220), (310), and (222), respectively, which indicates high crystallinity of the prepared ZIF-8 (Fig. 4.1c). The diffraction peaks located at 31.84°, 34.52°, 36.33°, 47.63°, 56.71°, 62.96°, 68.13°, and 69.18° corresponds to (100), (002), (101), (102), (110), (103), (200), (112), (201) and have been keenly indexed as hexagonal wurtzite phase of ZnO [61-63] (Fig. 4.1b), and further it also confirms the synthesized nanopowder was free of impurities as it does not contain any characteristics XRD peaks other than ZnO peaks. A peak at 27.5^{o} in the XRD of the ZCN 5 composite expected, which shows the incorporation of g-C_3N_4 with ZnO, but not observed.

4.2. FT-IR Analysis

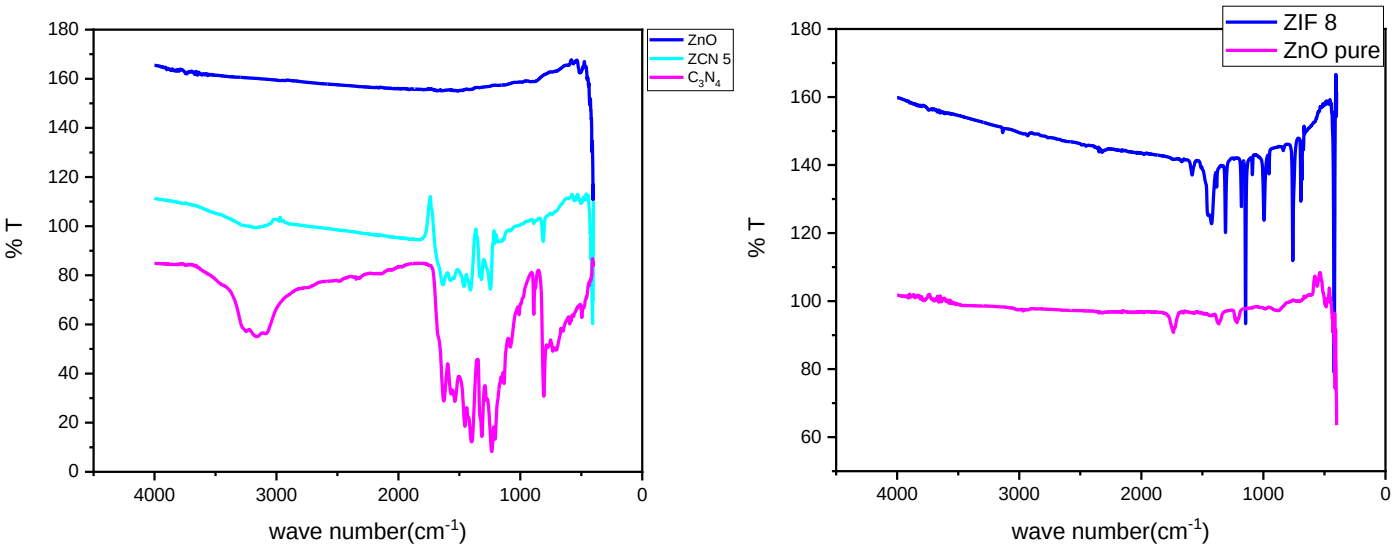

a b

Fig. 4.2. *FT-IR spectrum of g-C_3N_4(CN), ZnO from ZIF-8 and ZCN 5 composite*.

Fourier transform infrared (FT-IR) spectra of the g-C_3N_4(CN), ZnO from ZIF-8 and ZCN composite materials are shown in Fig. 4.2. For ZnO and ZnO composites, the peaks in the region from 400 to 560 cm^{-1} is corresponding to the bending vibrations of Zn–O bands [66, 67]. In the spectrum of g-C_3N_4, the peaks at 1243 and 1637 cm^{-1} correspond to the stretching vibrations of C−N and C=N, respectively [67]. The peaks at 810 cm^{-1} originate from the breathing mode of the s-triazine ring units [68]. The broad

absorption band at a high wave number around 3100–3400 cm^{-1} is attributed to the stretching vibration of N−H bonds in the $-NH_2$ and/or =N−H amines, as well as the hydroxyl groups of the chemisorbed and/or physisorbed H_2O molecules [67, 68]. It can be clearly seen that the main characteristic IR peaks of g-C_3N_4 exist in the ZnO@g-C_3N_4, suggesting that the structural features of g-C_3N_4 are maintained after the hybridization process, in good agreement with the XRD results. Additionally, the main characteristic peaks of g- C_3N_4 in the composites slightly shift to a high wavenumber. This red shift could be attributed to the fact that the extendedly conjugated system appears in the heterostructured composites [67,68]. The remarkable bands at 3135, 1635, 1583, 1458, 1424, 1382, 1310, 1146, 994, 758, 693 and 420 cm^{-1} represents the ZIF-8 sample. These FT-IR bands were consistent with the previously reported journals [64, 65].

4.3. UV-DRS Analysis

The absorption region of semiconducting photocatalyst is identified by the help of UV–Vis. Spectroscopy. Fig. 4.3. shows the UV-DRS data of ZnO, ZCN 5 composite and g-C_3N_4. The absorbtion wavelength of ZnO was similar to previous reported journals. The ZCN 5 composite shows slight redshift from derived ZnO. Therefore, the composite has absorption in the visible light region and hence expected have improved photocatalytic activity.

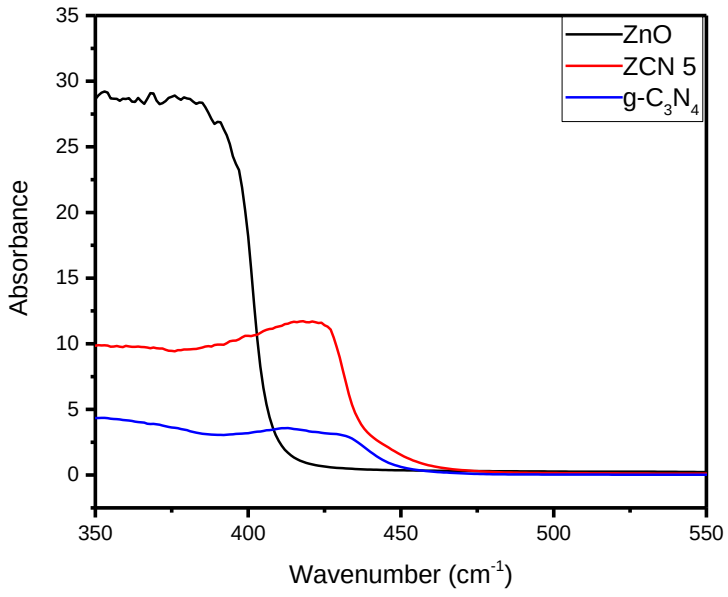

Fig. 4.3. *UV-DRS spectrum of ZnO, ZCN 5 and g-C_3N_4*

4.4. PL Analysis

It is evident from the PL spectra that g-C_3N_4 nano sheet has the highest strength, which is due to the high recombination rate of the electron hole. The composites display lower PL than g-C_3N_4. Lower the PL pressure, lower the rate of recombination of the electron hole. Therefore, composites should have a better catalyst property. The graph shows that ZCN 5 composite has lower PL intensity peak than that of other composites and shows a high photolytic activity as expected.

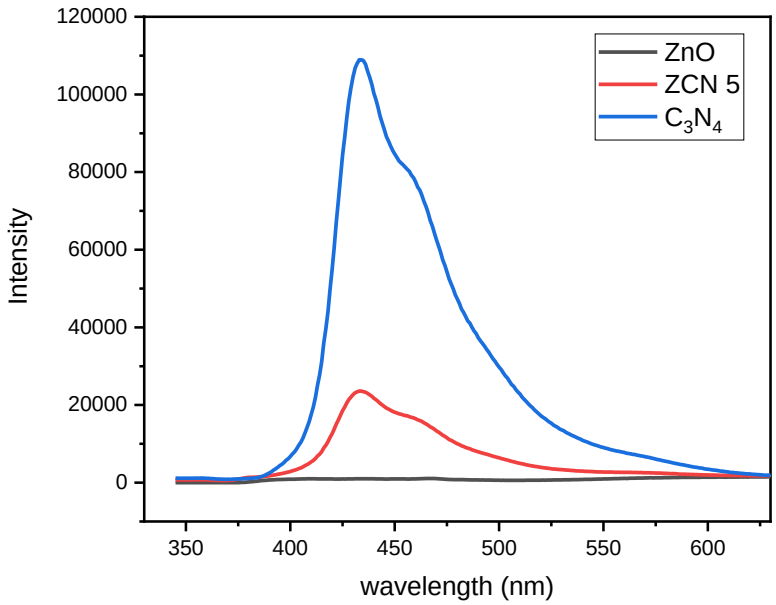

Fig. 4.4. *PL spectrum of ZCN 5 composite and g-C_3N_4 Nanosheet*

4.5. Photocatalytic activity of catalyst

The photocatalytic activity of photocatalyst is studied by analysing the degradation of Rhodamine B under sunlight irradiation. From the data a graph is plotted with C/C_0 against time (Fig. 4.5.). From the graph we could analyse that normal degradation of Rhodamine B under sunlight was too slow almost complete dye remained same as initial. The composite showed faster degradation than derived ZnO. It degraded about 90% of the dye within 80mins, whereas the ZnO showed about 70% degradation within the time.

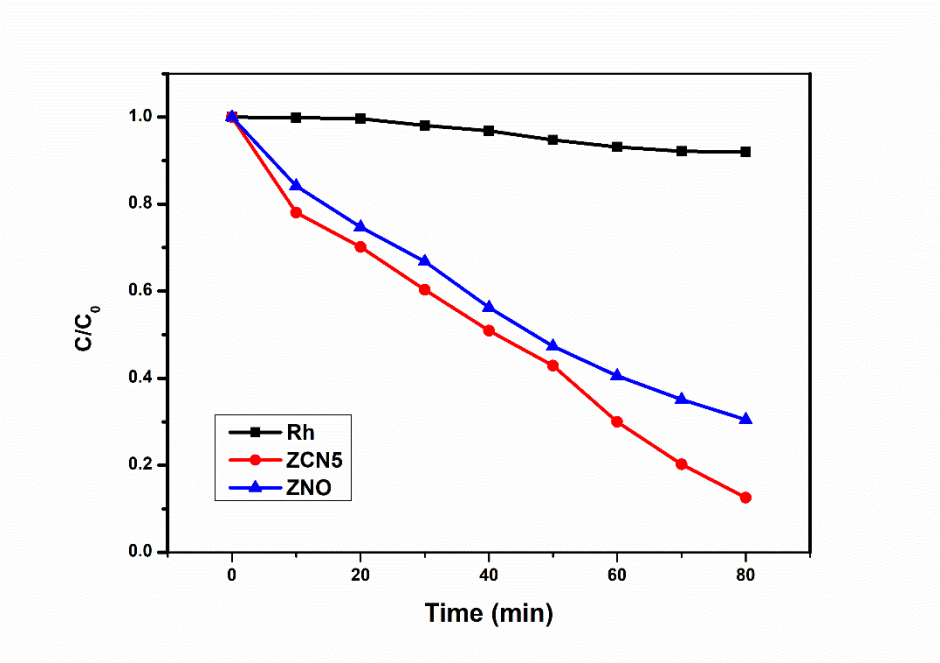

Fig. 4.5. *Photocatalytic degradation of Rh B*

5. CONCLUSION

In summary, we have synthesized an active photocatalyst composite ZnO@g-C_3N_4 (ZCN) by doping a non-metalic semiconductor polymeric carbon nitride(CN) with zeolitic imidazolate framework-8 (ZIF-8) derived ZnO and studied its photocatalytic application by degrading organic dye pollutant Rhodamine B under natural sunlight. The composite was characterized by FT-IR, XRD, UV-DRS and PL spectroscopy. The prepared composite (ZCN 5) showed higher photocatalytic efficiency under natural sunlight. About 90% of the dye was degraded within 80min of sunlight irradiation. The enhanced photocatalytic activity of the composite is due to the lower bandgap and lower electron recombination rate which enabled them to transfer electrons for photocatalytic degradation of dye. This project seems to bring a great deal of hope in processing dangerous and harmful chemical materials with minimal intermediates into safe end products at ambient temperature. Further methods may be used for future works to further improve their photocatalytic operation, such as isolation of the charge carrier, alteration of the energy band, etc.

6. REFERENCES

1. Ye, S., Yan, M., Tan, X., Liang, J., Zeng, G., Wu, H., Song, B., Zhou, C., Yang, Y. and Wang, H., 2019. Facile assembled biochar-based nanocomposite with improved graphitization for efficient photocatalytic activity driven by visible light. *Applied Catalysis B: Environmental*, 250, pp. 78-88.

2. Subiramaniyam, N.P., Vadivel, S., Kumaresan, S. and Vallalperuman, K., 2017. Fluorine-doped nanocrystalline ZnO powders prepared via microwave irradiation route as effective materials for photocatalyst. *Journal of Materials Science: Materials in Electronics*, *28*(21), pp. 16173-16180.

3. Pany, S. and Parida, K.M., 2015. A facile in situ approach to fabricate N, S-TiO_2/gC_3N_4 nanocomposite with excellent activity for visible light induced water splitting for hydrogen evolution. *Physical Chemistry Chemical Physics*, *17*(12), pp. 8070-8077.

4. Sobhani-Nasab, A., Behvandi, S., Karimi, M.A., Sohouli, E., Karimi, M.S., Gholipour, N., Ahmadi, F. and Rahimi-Nasrabadi, M., 2019. Synergetic effect of graphene oxide and C_3N_4 as co-catalyst for enhanced photocatalytic performance of dyes on $Yb_2(MoO_4)_3$/$YbMoO_4$ nanocomposite. *Ceramics International*, *45*(14), pp.17847-17858.

5. Lakshmi, K., Mathusalini, S., Arasakumar, T., Kadirvelu, K. and Mohan, P.S., 2017. Highly reactive lanthanum doped zinc oxide nanofiber photocatalyst for effective decontamination of methyl parathion. *Journal of Materials Science: Materials in Electronics*, *28*(17), pp. 12944-12955.

6. Peymani-Motlagh, S.M., Sobhani-Nasab, A., Rostami, M., Sobati, H., Eghbali-Arani, M., Fasihi-Ramandi, M., Ganjali, M.R. and Rahimi-Nasrabadi, M., 2019. Assessing the magnetic, cytotoxic and photocatalytic influence of incorporating Yb^{3+} or Pr^{3+} ions in cobalt–nickel ferrite. *Journal of Materials Science*: *Materials in Electronics, 30*(7), pp. 6902-6909.

7. Kooshki, H., Sobhani-Nasab, A., Eghbali-Arani, M., Ahmadi, F., Ameri, V. and Rahimi-Nasrabadi, M., 2019. Eco-friendly synthesis of $PbTiO_3$ nanoparticles and $PbTiO_3$/carbon quantum dots binary nano-hybrids for enhanced photocatalytic performance under visible light. *Separation and Purification Technology*, *211*, pp. 873-881.

8. Zhao, L., Zhong, C., Wang, Y., Wang, S., Dong, B. and Wan, L., 2015. Ag nanoparticle-decorated 3D flower-like TiO2 hierarchical microstructures composed of ultrathin nanosheets and enhanced photoelectrical conversion properties in dye-sensitized solar cells. *Journal of Power Sources*, *292*, pp. 49-57.

9. Qu, Y. and Duan, X., 2013. Progress, challenge and perspective of heterogeneous photocatalysts. *Chemical Society Reviews*, *42*(7), pp. 2568-2580.

10. Liu, X., Zhong, J., Li, J., Hu, W., Wang, Q., Wang, G., Song, J., Liu, K., Huang, K., Wu, S. and Yang, R., 2016. Enhanced simulated sun light photocatalytic activity of α-Fe_2O_3 modified g-C_3N_4 prepared in-situ. *Journal of Advanced Oxidation Technologies*, *19*(1), pp. 27-33.

11. Ren, S., Chen, C., Zhou, Y., Dong, Q. and Ding, H., 2017. The α-Fe_2O_3/g-C_3N_4 composite as an efficient heterogeneous catalyst with combined Fenton and photocatalytic effects. *Research on Chemical Intermediates*, *43*(5), pp. 3307-3323.

12. Rai, V.K., Verma, F., Mahata, S., Bhardiya, S.R., Singh, M. and Rai, A., 2019. Metal Doped-C_3N_4/Fe_2O_4: Efficient and Versatile Heterogenous Catalysts for Organic Transformations. *Current Organic Chemistry*, *23*(12), pp. 1284-1306.

13. Preethi, V. and Kanmani, S., 2013. Photocatalytic hydrogen production. *Materials Science in Semiconductor Processing*, *16*(3), pp. 561-575.

14. Karimipour, M., Sadeghian, M. and Molaei, M., 2018. Fabrication of white light LED photocatalyst ZnO–rGO heteronanosheet hybrid materials. *Journal of Materials Science: Materials in Electronics*, *29*(16), pp. 13782-13793.

15. Li, X., Liu, D., Shi, Z. and Yang, J., 2019. Effect of Ag 2 S shell thickness on the photocatalytic properties of ZnO/Ag_2S core–shell nanorod arrays. *Journal of Materials Science*, *54*(2), pp. 1226-1235.

16. Li, J. and Wu, N., 2015. Semiconductor-based photocatalysts and photoelectrochemical cells for solar fuel generation: a review. *Catalysis Science & Technology*, *5*(3), pp.1360-1384.

17. Zhang, P., Zhang, J. and Gong, J., 2014. Tantalum-based semiconductors for solar water splitting. *Chemical Society Reviews*, *43*(13), pp. 4395-4422.;

18. Zhang, P., Zhang, J. and Gong, J., 2014. Tantalum-based semiconductors for solar water splitting. *Chemical Society Reviews, 43*(13), pp. 4395-4422.

19. Gershon, T., Shin, B., Bojarczuk, N., Hopstaken, M., Mitzi, D.B. and Guha, S., 2015. The role of sodium as a surfactant and suppressor of non-radiative recombination at internal surfaces in Cu2ZnSnS4. *Advanced Energy Materials, 5*(2), pp.1400849.

20. Low, J., Jiang, C., Cheng, B., Wageh, S., Al-Ghamdi, A.A. and Yu, J., 2017. A review of direct Z-scheme photocatalysts. *Small Methods*, *1*(5), pp.1700080.

21. Simon, T., Carlson, M.T., Stolarczyk, J.K. and Feldmann, J., 2016. Electron transfer rate vs recombination losses in photocatalytic H2 generation on Pt-decorated CdS nanorods. *ACS energy letters, 1*(6), pp.1137-1142.

22. Dias, P., Lopes, T., Andrade, L. and Mendes, A., 2014. Temperature effect on water splitting using a Si-doped hematite photoanode. *Journal of Power Sources*, *272*, pp.567-580.

23. Schiavello, M., 1988. *Photocatalysis and environment*. Springer Netherlands.

24 Serpone, N. and Pelizzetti, E., 1989. *Photocatalysis: fundamentals and applications*. Wiley Interscience.

25. Ibusuki, T., Kutsuna, S., Takeuchi, K., Shin-Kai, K., Samamato, T. and Miyamato, M., 1993. Photocatalytic Purification and Treatment of Water and Air, ed. DF Ollis and H. Al-Ekabi.

26. Legrini, O., Oliveros, E. and Braun, A.M., 1993. Photochemical processes for water treatment. *Chemical reviews*, *93*(2), pp. 671-698.

27. Herrmann, J.M., Guillard, C. and Pichat, P., 1993. Heterogeneous photocatalysis: an emerging technology for water treatment. *Catalysis Today*, *17*(1-2), pp. 7-20.

28. Bahnemann, D., Cunningham, J., Fox, M.A., Pelizzetti, E., Pichat, P. and Serpone, N., 1994. Photocatalytic treatment of waters. *Aquatic and surface photochemistry*, pp. 261-316.

29. Zhang, T. and Lin, W., 2014. Metal–organic frameworks for artificial photosynthesis and photocatalysis. *Chemical Society Reviews*, *43*(16), pp. 5982-5993.

30. Čejka, J., 2012. Metal-Organic Frameworks. Applications from Catalysis to Gas Storage. Edited by David Farrusseng. *Angewandte Chemie International Edition*, *51*(20), pp. 4782-4783.

31. Klinowski., J., Paz., F. A., Silva., P., & Rocha, J. (2011). Microwave-Assisted Synthesis of Metal–Organic Frameworks. *Dalton Transactions*, 321-330.

32. Zaho, Y., 2016. Emerging Applications of Metal−Organic Frameworks and Covalent Organic Frameworks. *Chemistry of Materials*, 8079-8081.

33. Sholl, D.S. and Lively, R.P., 2015. Defects in metal–organic frameworks: challenge or opportunity?. *The journal of physical chemistry letters*, *6*(17), pp. 3437-3444.

34. Chedid, G. and Yassin, A., 2018. Recent trends in covalent and metal organic frameworks for biomedical applications. *Nanomaterials*, *8*(11), pp. 916.

35. Steenhaut, T., Hermans, S. and Filinchuk, Y., 2020. Green synthesis of a large series of bimetallic MIL-100 (Fe, M) MOFs. *New Journal of Chemistry*, *44*(10), pp. 3847-3855.

36. Steenhaut, T., Grégoire, N., Barozzino-Consiglio, G., Filinchuk, Y. and Hermans, S., 2020. Mechanochemical defect engineering of HKUST-1 and impact of the resulting defects on carbon dioxide sorption and catalytic cyclopropanation. *RSC Advances*, *10*(34), pp. 19822- 19831.

37. Cruz, A.J., Stassen, I., Krishtab, M., Marcoen, K., Stassin, T., Rodríguez-Hermida, S., Teyssandier, J., Pletincx, S., Verbeke, R., Rubio-Giménez, V. and Tatay, S., 2019. Integrated cleanroom process for the vapor-phase deposition of large-area zeolitic imidazolate framework thin films. *Chemistry of Materials*, *31*(22), pp.9462-9471.

38. Remya, V.R. and Kurian, M., 2019. Synthesis and catalytic applications of metal–organic frameworks: a review on recent literature. *International Nano Letters*, *9*(1), pp. 17-29.

39. Zhang, H., Liu, G., Shi, L., Liu, H., Wang, T. and Ye, J., 2016. Engineering coordination polymers for photocatalysis. *Nano Energy, 22*, pp. 149-168.

40. Dhakshinamoorthy, A., Asiri, A.M. and Garcia, H., 2016. Metal–organic framework (MOF) compounds: photocatalysts for redox reactions and solar fuel production. *Angewandte Chemie International Edition*, *55*(18), pp. 5414-5445.

41. Zeng, L., Guo, X., He, C. and Duan, C., 2016. Metal–organic frameworks: versatile materials for heterogeneous photocatalysis. *ACS Catalysis*, *6*(11), pp. 7935-7947.

42. He, J., Zhang, Y., He, J., Zeng, X., Hou, X. and Long, Z., 2018. Enhancement of photoredox catalytic properties of porphyrinic metal–organic frameworks based on titanium incorporation via post-synthetic modification. *Chemical Communications*, *54*(62), pp. 8610-8613.

43. Nasalevich, M.A., Van der Veen, M., Kapteijn, F. and Gascon, J., 2014. Metal–organic frameworks as heterogeneous photocatalysts: advantages and challenges. *CrystEngComm*, *16*(23), pp. 4919-4926.

44. Wang, D., Wang, M. and Li, Z., ACS Catal. 2015, 5, 6852. *Google Scholar*| *Crossref*.

45. Park, K.S., Ni, Z., Côté, A.P., Choi, J.Y., Huang, R., Uribe-Romo, F.J., Chae, H.K., O'Keeffe, M. and Yaghi, O.M., 2006. Exceptional chemical and thermal stability of zeolitic imidazolate frameworks. *Proceedings of the National Academy of Sciences*, *103*(27), pp. 10186-10191.

46. Fairen-Jimenez, D., Moggach, S.A., Wharmby, M.T., Wright, P.A., Parsons, S. and Duren, T., 2011. Opening the gate: framework flexibility in ZIF-8 explored by experiments and simulations. *Journal of the American Chemical Society*, *133*(23), pp. 8900-8902.

47. Wang, B., Côté, A.P., Furukawa, H., O'Keeffe, M. and Yaghi, O.M., 2008. Colossal cages in zeolitic imidazolate frameworks as selective carbon dioxide reservoirs. *Nature*, *453*(7192), pp. 207-211.

48. Wang, F., Tan, Y.X., Yang, H., Zhang, H.X., Kang, Y. and Zhang, J., 2011. A new approach towards tetrahedral imidazolate frameworks for high and selective CO_2 uptake. *Chemical Communications*, *47*(20), pp. 5828-5830.

49. Tranchemontagne, D.J., Hunt, J.R. and Yaghi, O.M., 2008. Room temperature synthesis of metal-organic frameworks: MOF-5, MOF-74, MOF-177, MOF-199, and IRMOF-0. *Tetrahedron*, *64*(36), pp. 8553-8557.

50. Cravillon, J., Münzer, S., Lohmeier, S.J., Feldhoff, A., Huber, K. and Wiebcke, M., 2009. Rapid room-temperature synthesis and characterization of nanocrystals of a prototypical zeolitic imidazolate framework. *Chemistry of Materials*, *21*(8), pp.1410-1412.

51. Tran, U.P.N., Le, K.K.A., Phan, N.T.S. and Catal, A.C.S., 2012. 1, 120–127; c) CM Miralda, EE Macias, M. *Zhu, P. Ratnasamy, MA Carreon, ACS Catal*, *2*, pp. 180-183.

52. Bux, H., Liang, F., Li, Y., Cravillon, J., Wiebcke, M. and Caro, J., 2009. Zeolitic imidazolate framework membrane with molecular sieving properties by microwave-assisted solvothermal synthesis. *Journal of the American Chemical Society*, *131*(44), pp. 16000-16001.

53. Polyzoidis, A., Altenburg, T., Schwarzer, M., Loebbecke, S. and Kaskel, S., 2016. Continuous microreactor synthesis of ZIF-8 with high space–time-yield and tunable particle size. *Chemical Engineering Journal*, *283*, pp.971-977.54. M. A. Nasalevich, M. van der Veen, F. Kapteijn and J. Gascon, CrystEngComm, 2014, 16, pp. 4919–4926.

55. Yang, X., Wen, Z., Wu, Z. and Luo, X., 2018. Synthesis of ZnO/ZIF-8 hybrid photocatalysts derived from ZIF-8 with enhanced photocatalytic activity. *Inorganic Chemistry Frontiers*, *5*(3), pp. 687-693.

56. Wang, H. and Jin, Z., 2018. Design and synthesis of polymeric carbon nitride@ zeolitic imidazolate frameworks (CoWS) semiconductor junction nanowires for efficient photocatalytic hydrogen evolution. *New Journal of Chemistry*, *42*(21), pp. 17396-17406.

57. Kumaresan, N., Sinthiya, M.M.A., Kumar, M.P., Ravichandran, S., Babu, R.R., Sethurman, K. and Ramamurthi, K., 2020. Investigation on the g-C3N4 encapsulated ZnO nanorods heterojunction coupled with GO for effective photocatalytic activity under visible light irradiation. *Arabian Journal of Chemistry*, *13*(1), pp. 2826-2843.

58. Rasheed, H.U., Lv, X., Wei, W., Yaseen, W., Ullah, N., Xie, J. and Zhu, W., 2019. Synthesis and studies of ZnO doped with g-C3N4 nanocomposites for the degradation of tetracycline hydrochloride under the visible light irradiation. *Journal of Environmental Chemical Engineering*, *7*(3), p. 103152.

59. Zheng, H.B., Wu, D., Wang, Y.L., Liu, X.P., Gao, P.Z., Liu, W., Wen, J. and Rebrov, E.V., 2020. One-step synthesis of ZIF-8/ZnO composites based on coordination defect strategy and its derivatives for photocatalysis. *Journal of Alloys and Compounds*, pp. 155219.

60. Jing, Y., Wang, J., Yu, B., Lun, J., Cheng, Y., Xiong, B., Lei, Q., Yang, Y., Chen, L. and Zhao, M., 2017. A MOF-derived ZIF-8@ Zn 1− x Ni x O photocatalyst with enhanced photocatalytic activity. *RSC Advances*, *7*(67), pp. 42030-42035.

61. Zhou, J., Zhao, F., Wang, Y., Zhang, Y. and Yang, L., 2007. Size-controlled synthesis of ZnO nanoparticles and their photoluminescence properties. *Journal of luminescence*, *122*, pp. 195-197.

62. Khoshhesab, Z.M., Sarfaraz, M. and Asadabad, M.A., 2011. Preparation of ZnO nanostructures by chemical precipitation method. *Synthesis and Reactivity in Inorganic, Metal-Organic, and Nano-Metal Chemistry*, *41*(7), pp. 814-819.

63. JCPDS, P.D.F., 1977. Alphabetical Index. *Inorganic Compounds, International Centre for Diffraction Data, Newtown Square, Pa, USA*.

64. Park, K.S., Ni, Z., Côté, A.P., Choi, J.Y., Huang, R., Uribe-Romo, F.J., Chae, H.K., O'Keeffe, M. and Yaghi, O.M., 2006. Exceptional chemical and thermal stability of zeolitic imidazolate frameworks. *Proceedings of the National Academy of Sciences*, *103*(27), pp. 10186-10191.

65. Ordonez, M.J.C., Balkus Jr, K.J., Ferraris, J.P. and Musselman, I.H., 2010. Molecular sieving realized with ZIF-8/Matrimid® mixed-matrix membranes. *Journal of Membrane Science*, *361* (1-2), pp. 28-37.

66. Jo, W.K. and Selvam, N.C.S., 2015. Enhanced visible light-driven photocatalytic performance of ZnO–g-C3N4 coupled with graphene oxide as a novel ternary nanocomposite. *Journal of hazardous materials*, *299*, pp. 462-470.

67. Kumar, S., Baruah, A., Tonda, S., Kumar, B., Shanker, V. and Sreedhar, B., 2014. Cost-effective and eco-friendly synthesis of novel and stable N-doped ZnO/gC_3N_4 core–shell nanoplates with excellent visible-light responsive photocatalysis. *Nanoscale*, *6*(9), pp. 4830-4842.

68. Wang, Y., Shi, R., Lin, J. and Zhu, Y., 2011. Enhancement of photocurrent and photocatalytic activity of ZnO hybridized with graphite-like C_3N_4. *Energy & Environmental Science*, *4*(8), pp. 2922-2929.